NURBS-based numerical proxies for red blood cells and circulating tumor cells in microscale blood flow

Hugo Casquero[a,*], Carles Bona-Casas[b], Hector Gomez[a]

[a]*Departamento de Métodos Matemáticos, Universidade da Coruña, Campus de A Coruña, 15071, A Coruña, Spain.*
[b]*Departament de Física, Universitat de les Illes Balears, 07122, Palma de Mallorca, Spain*

Abstract

We explore the use of NURBS-based immersed fluid-structure interaction algorithms to model the dynamics and rheology of red blood cells (RBCs) and nucleated cells. Prime examples of cells with nucleus that are relevant to this study are white blood cells (WBCs) and circulating tumor cells (CTCs). In this work, RBCs are modeled as thin solid membranes called *capsules*. To model cells with nucleus we introduce the concept of *compound capsule* which explicitly takes into account the nucleus as a bulky deformable solid. Our results indicate that to reproduce the behavior of RBCs in shear and parabolic flows, it is crucial to accurately solve the mass conservation equation near the fluid-solid interface. We show results of hyperelastic capsules and compound capsules in two- and three-dimensional settings. Finally, taking advantage of the geometric flexibility of our method, we simulate how a CTC passes through a narrowing. This is a feature of CTCs that has recently triggered excitement in the experimental community.

Keywords:
Isogeometric analysis, Immersed fluid-structure interaction, Hyperelastic compound capsules, Tank-treading motion, Tumbling motion, Fåhræus-Lindqvist Effect

1. Introduction

Blood is a complex fluid that is primarily made of blood plasma and red blood cells (RBCs). The concentration of RBCs (hematocrit) in a healthy human body is in average 45% of the blood volume. The remaining formed elements of blood such as, e.g., white blood cells (WBCs) and platelets, add up to less than 1% of the total blood volume. The mechanical behavior of blood depends strongly on the scale of study. In large vessels with a diameter greater than 500 µm, considering blood as a Newtonian fluid with a constant viscosity is sufficiently accurate for most applications. However, in vessels with smaller diameters, blood behaves as a non-Newtonian fluid. In fact, to be able to match experimental

*Corresponding author.
Email address: hugo.casquero@udc.es (Hugo Casquero)

results of blood flow in cylindrical tubes with Poiseuille's law, it is necessary to define an *apparent viscosity* that depends at least on the tube's diameter and the hematocrit. This phenomenon is known as the Fåhræus-Lindqvist effect [1].

In most cases, RBCs are the blood constituent principally responsible for the dynamics and rheology of blood, which is related with the fact that RBCs are more numerous and more deformable than the remaining formed elements of blood. One way to study microscale blood flow is to explicitly model RBCs. This is the approach chosen in the present work and it leads to a fluid-structure interaction (FSI) problem that we solve using an immersed approach. A RBC is composed by a lipid bilayer membrane with an attached spectrin network called cytoskeleton which encapsulates a concentrated hemoglobin solution that behaves as a Newtonian incompressible fluid. Under physiological conditions, both the RBC volume and external area are nearly constant. In a quiescent fluid, healthy RBCs have a biconcave shape. Nevertheless, under nonequilibrium conditions such us, e.g., pure shear flow and parabolic flow, RBCs exhibit a variety of interesting shapes and motions [2, 3]. In the last decades, the reproduction of experimental shapes and motions has been the most widespread benchmark test used in order to evaluate the accuracy and efficiency of different RBC models in blood flow*. The two most common continuum-based approaches for modeling RBCs are the so-called *vesicles* [5, 6, 7] and *capsules* [8]. Vesicles consider the bending resistance of the lipid bilayer membrane which can be directly controlled through a parameter called bending rigidity, but they neglect the shear resistance of the cytoskeleton. Capsules consider both bending and shear resistances, but both types of resistances are usually controlled through the same parameter, namely, the shear modulus. In this work, we use capsules as our model for RBCs.

Blood plasma behaves as a Newtonian incompressible fluid whose average density and dynamic viscosity are $1.025\,\mathrm{g/cm^3}$ and $1.2\,\mathrm{mPa\ s}$, respectively [9]. Due to the low values of the Reynolds number usually encountered in microcirculation problems, it is quite common to assume Stokes flow to model blood plasma at small scales. However, recent findings show that inertial effects do play an important role in microcirculation, especially when the flow domain is curved [10, 11]. These observations are giving rise to an entirely new field call *inertial microfluidics* and are expected to have practical applications in the next few years. Motivated by this experimental evidence, we do not assume Stokes flow, but solve the Navier-Stokes equations using the variational multiscale (VMS) technique [12, 13, 14].

In the last few years, the continuum-based modeling of WBCs has received increasing attention. The goal is to elucidate a plethora of open questions about flows that involve both RBCs and WBCs. Besides of a membrane, a WBC contains a nucleus, organelles, and fibers, which are suspended in a viscous cytosol [15]. Therefore, modeling WBCs either as bulky bodies or using the same models used for RBCs (e.g., vesicles or capsules) is not accurate in a number of situations. In [16], a model for WBCs is proposed under the assumption that the behavior of a WBC is dominated by its nucleus, its viscous cytosol,

*For a thorough discussion of the different types of models used for RBCs, the interested reader is remitted to [4].

and its membrane, that is, the organelles and other internal constituents are neglected. Ref. [16] introduces the concept of *compound vesicles* in which the membrane is modeled as a vesicle (i.e., they only consider bending resistance) and the nucleus is modeled as a rigid body (i.e., they neglect its strains). The modeling of other types of nucleated cells, e.g., circulating tumor cells (CTCs) is also an appealing subject. CTCs are cancerous cells that escape from the tumor, enter the circulatory system through a process called intravasation and acquire the ability to survive in this new environment. Eventually, some of these cells may extravasate, that is, leave the circulatory system, settle in a new organ and possibly create a secondary tumor. This process is part of the so-called metastatic cascade. We believe that understanding the behavior of CTCs in microcirculation would lead to a deeper understanding of the metastatic cascade which could help to develop therapies to stop cancer spreading [17]. It may also permit to design devices that allow to isolate CTCs from a blood sample with diagnostic purposes.

In this work, we use a NURBS-based immersed FSI approach to study the behavior of capsules in shear and parabolic flows. Our numerical results are compared with experimental results for RBCs. Good agreement is found as long as the incompressibility constraint is adequately satisfied near the fluid-solid interface. Ensuring that the incompressibility constraint is satisfied is quite challenging due to the assumption of continuous pressure across the fluid-solid interface which is done in all immersed methods that we are aware of. Moreover, handling the large strains undergone by the numerical proxies of RBCs is one of the main bottlenecks of mesh-based immersed FSI approaches. In [18, 19], the authors claim that piecewise linear Lagrange polynomials cannot deal with the large strains found in their simulations and they propose to use the meshfree reproducing kernel particle method for representing the capsules instead [20, 21]. In our case, the higher inter-element continuity of NURBS gives us sufficient robustness [22] to handle the large strains undergone by the capsules in all of our simulations. In this paper, we introduce the concept of *compound capsules* to model nucleated cells. A compound capsule is formed by a capsule, an incompressible Newtonian fluid enclosed by the capsule, and a bulky deformable solid suspended in the fluid, which represent the membrane, the cytosol, and the nucleus of the cell, respectively. The dynamics of compound capsules in shear flow are analyzed in two- and three-dimensional settings. Our results are in agreement with those of compound vesicles. Additionally, the geometric flexibility of our immersed approach enables us to solve problems on non-trivial geometries.

The paper is organized as follows: Section 2 describes our FSI modeling framework and emphasizes the main challenges faced when an immersed approach is used. Section 3 studies the dynamics of capsules and compound capsules in shear flows. In Section 4, we focus on the behavior of RBCs and CTCs in parabolic flows. Section 5 presents our conclusions and future directions of work.

2. FSI simulation using an immersed approach

Our FSI formulation at the continuous and discrete levels was thoroughly derived in our two earlier works [23, 24]. In this Section, we summarize our hybrid variational-collocation

immersed method for FSI and focus on a number of important subjects, namely, how to improve local mass conservation close to the fluid-solid interface, how to alleviate the issue of suboptimal quadrature rules that arises in immersed FSI through higher inter-element continuity, the coupling strategy, and the nonlinear and linear solvers used for the final system of algebraic equations.

2.1. Governing equations

Let $d = \{2, 3\}$ be the number of spatial dimensions. Let $\Omega_t^1 \subset \mathbb{R}^d$ and $\Omega_t^2 \subset \mathbb{R}^d$ be two open sets that represent the time-dependent domains occupied by a viscous incompressible fluid and a hyperelastic incompressible solid, respectively. Γ_t^1 and Γ_t^2 are their corresponding boundaries. These two regions meet at the fluid-solid interface $\Gamma_t^I = \overline{\Omega_t^1} \cap \overline{\Omega_t^2}$. Let $\Omega \subset \mathbb{R}^d$ be an open set that represents the domain occupied by both the fluid and the solid, that is, $\overline{\Omega} = \overline{\Omega_t^1 \cup \Omega_t^2}$. In all the simulations presented in this paper, Ω is time independent. Therefore, we will assume that Ω is fixed in time to simplify the description of our algorithm. The boundary of Ω is denoted by Γ. Let $\boldsymbol{v} : \Omega \times (0,T) \mapsto \mathbb{R}^d$, $p : \Omega \times (0,T) \mapsto \mathbb{R}$, and $\boldsymbol{u}_2 : \Omega_0^2 \times (0,T) \mapsto \mathbb{R}^d$ denote the Eulerian velocity, the Eulerian pressure, and the Lagrangian displacement, respectively, where $(0,T)$ is the time interval of interest and Ω_0^2 is a reference configuration of Ω_t^2. Let $\boldsymbol{X} \in \Omega_0^2$, $\boldsymbol{x} \in \Omega$, and $\boldsymbol{\varphi} : \Omega_0^2 \times (0,T) \mapsto \Omega_t^2$ be a material point, a spatial point, and the deformation mapping $\boldsymbol{\varphi}(\boldsymbol{X}, t) = \boldsymbol{X} + \boldsymbol{u}_2(\boldsymbol{X}, t)$, respectively.

The three equations that define our problem are the linear momentum balance equation, the mass conservation equation, and the kinematic relation between the Eulerian velocity and the Lagrangian displacement, i.e.,

$$\rho_1 \left(\frac{\partial \boldsymbol{v}}{\partial t} + \boldsymbol{v} \cdot \nabla_{\boldsymbol{x}} \boldsymbol{v} \right) = \nabla_{\boldsymbol{x}} \cdot \boldsymbol{\sigma}_1 + \rho_1 \boldsymbol{g} + \boldsymbol{\mathcal{F}} \qquad \text{in} \quad \Omega \times (0,T) \ , \tag{1}$$

$$\nabla_{\boldsymbol{x}} \cdot \boldsymbol{v} = 0 \qquad \text{in} \quad \Omega \times (0,T) \ , \tag{2}$$

$$\frac{\partial \boldsymbol{u}_2}{\partial t} = \boldsymbol{v} \qquad \text{in} \quad \Omega_t^2 \times (0,T) \ , \tag{3}$$

with

$$\boldsymbol{\mathcal{F}} = \begin{cases} 0, & \boldsymbol{x} \in \Omega_t^1 \\ (\rho_1 - \rho_2) \left(\dfrac{\partial \boldsymbol{v}}{\partial t} + \boldsymbol{v} \cdot \nabla_{\boldsymbol{x}} \boldsymbol{v} - \boldsymbol{g} \right) + \nabla_{\boldsymbol{x}} \cdot (\boldsymbol{\sigma}_2 - \boldsymbol{\sigma}_1) \, , & \boldsymbol{x} \in \Omega_t^2 \end{cases} \ , \tag{4}$$

and constitutive laws

$$\boldsymbol{\sigma}_1 = -p\boldsymbol{I} + 2\mu \nabla_{\boldsymbol{x}}^{\text{sym}} \boldsymbol{v} \ , \tag{5}$$

$$\boldsymbol{\sigma}_2 = -p\boldsymbol{I} + \boldsymbol{F}\boldsymbol{S}\boldsymbol{F}^T / J \ . \tag{6}$$

Here, ρ_1 and ρ_2 are the fluid and solid densities, respectively, $\boldsymbol{\sigma}_1$ and $\boldsymbol{\sigma}_2$ are the fluid and solid Cauchy stress tensors, respectively, $\boldsymbol{g}$ is an external body force acting on the system, $\boldsymbol{I}$ denotes the identity tensor in $\mathbb{R}^{d \times d}$, μ is the dynamic viscosity of the fluid, $\nabla_{\boldsymbol{x}}^{\text{sym}}(\cdot)$ is the symmetric gradient operator given by $\nabla_{\boldsymbol{x}}^{\text{sym}} \boldsymbol{v} = (\nabla_{\boldsymbol{x}} \boldsymbol{v} + \nabla_{\boldsymbol{x}} \boldsymbol{v}^T)/2$, $\boldsymbol{F} : \Omega_0^2 \times (0,T) \mapsto \mathbb{R}^{d \times d}$ is the deformation gradient given by $\boldsymbol{F} = \nabla_{\boldsymbol{X}} \boldsymbol{\varphi} = \boldsymbol{I} + \nabla_{\boldsymbol{X}} \boldsymbol{u}_2$, $\boldsymbol{S}$ denotes the second

Piola-Kirchhoff stress tensor of the considered hyperelastic incompressible solid, and $J = \det(\boldsymbol{F})$ is the Jacobian determinant. At the continuous level, $J = 1$ because the solid is incompressible.

In order to achieve a well-posed FSI problem, we need to impose suitable initial and boundary conditions. Regarding initial conditions, the Eulerian velocity and Lagrangian displacement need to be given at the initial time. To simplify the definition of boundary conditions, we consider that the solid is fully immersed in the fluid, which is the case of interest for RBCs and CTCs. In this scenario, the boundary of the solid coincides with the fluid-solid interface ($\Gamma_t^2 = \Gamma_t^I$) and we impose two boundary conditions at the interface, namely, the no-slip boundary condition and the stress compatibility between the fluid and solid Cauchy stress tensors. The no-slip boundary condition is imposed through Eq. (3) and the stress compatibility condition will be naturally enforced by the variational form of (1). On the boundary of the fluid $\Gamma_t^1 = \Gamma$, we assume the standard split in Dirichlet boundary conditions on Γ_D and Neumann boundary conditions on Γ_N. The sets Γ_D and Γ_N satisfy the relations $\Gamma = \Gamma_D \cup \Gamma_N$ and $\Gamma_D \cap \Gamma_N = \emptyset$.

Eq. (3) will be discretized in space using isogeometric collocation [25, 26, 27, 28], therefore, it is not necessary to recast it in weak form. However, Eqs. (1) and (2) will be discretized in space using a weighted residual formulation, viz., the VMS approach proposed in [14]. The basic idea behind the VMS technique is to split the velocity and the pressure into two components, namely, $\boldsymbol{v} = \widetilde{\boldsymbol{v}} + \boldsymbol{v}'$ and $p = \widetilde{p} + p'$. Here, $\widetilde{\boldsymbol{v}}$ and $\widetilde{p}$ are finite-dimensional coarse-scale components while $\boldsymbol{v}'$ and p' are infinite-dimensional fine-scale components. Then, we multiply Eqs. (1) and (2) by weight functions $\widetilde{\boldsymbol{w}}$ and $\widetilde{q}$, respectively, integrate over Ω, and perform various mathematical operations described in detail in [14]. Following the aforementioned steps, we derive the following weak formulation of Eqs. (1) and (2):

$$B^{ED}\left(\{\widetilde{\boldsymbol{w}}, \widetilde{q}\}, \{\widetilde{\boldsymbol{v}} + \boldsymbol{v}', \widetilde{p} + p'\}\right) - L^{ED}\left(\widetilde{\boldsymbol{w}}\right) + B^{LD}\left(\widetilde{\boldsymbol{w}}, \widetilde{\boldsymbol{v}}; \boldsymbol{u}_2\right) = 0 \ . \tag{7}$$

with

$$\begin{aligned} B^{ED}\left(\{\widetilde{\boldsymbol{w}}, \widetilde{q}\}, \{\widetilde{\boldsymbol{v}} + \boldsymbol{v}', \widetilde{p} + p'\}\right) = & \left(\widetilde{\boldsymbol{w}}, \frac{\partial \widetilde{\boldsymbol{v}}}{\partial t} + \widetilde{\boldsymbol{v}} \cdot \nabla_{\boldsymbol{x}} \widetilde{\boldsymbol{v}}\right)_{\Omega} \\ & - \left(\nabla_{\boldsymbol{x}} \cdot \widetilde{\boldsymbol{w}}, \widetilde{p}\right)_{\Omega} + \left(\nabla_{\boldsymbol{x}}^{\mathrm{sym}} \widetilde{\boldsymbol{w}}, 2\nu \nabla_{\boldsymbol{x}}^{\mathrm{sym}} \widetilde{\boldsymbol{v}}\right)_{\Omega} \\ & + \left(\widetilde{q}, \nabla_{\boldsymbol{x}} \cdot \widetilde{\boldsymbol{v}}\right)_{\Omega} + \left(\widetilde{\boldsymbol{w}}, \boldsymbol{v}' \cdot \nabla \widetilde{\boldsymbol{v}}\right)_{\Omega} \\ & - \left(\nabla_{\boldsymbol{x}} \widetilde{\boldsymbol{w}}, (\widetilde{\boldsymbol{v}} + \boldsymbol{v}') \otimes \boldsymbol{v}'\right)_{\Omega} - \left(\nabla_{\boldsymbol{x}} \cdot \widetilde{\boldsymbol{w}}, p'\right)_{\Omega} \\ & - \left(\nabla_{\boldsymbol{x}} \widetilde{q}, \boldsymbol{v}'\right)_{\Omega} \ , \end{aligned} \tag{8}$$

$$L^{ED}\left(\widetilde{\boldsymbol{w}}\right) = \left(\widetilde{\boldsymbol{w}}, \boldsymbol{g}\right)_{\Omega} + \left(\widetilde{\boldsymbol{w}}, \boldsymbol{h}/\rho_1\right)_{\Gamma_N} \ , \tag{9}$$

$$
\begin{aligned}
B^{LD}\left(\widetilde{\boldsymbol{w}},\widetilde{\boldsymbol{v}};\boldsymbol{u}_2\right) = &-\left(\widetilde{\boldsymbol{w}},\left(1-\frac{\rho_2}{\rho_1}\right)\frac{\partial\widetilde{\boldsymbol{v}}}{\partial t}\right)_{\Omega_0^2}\\
&-\left(\widetilde{\boldsymbol{w}},\left(1-\frac{\rho_2}{\rho_1}\right)\widetilde{\boldsymbol{v}}\cdot\nabla_{\boldsymbol{x}}\widetilde{\boldsymbol{v}}\right)_{\Omega_0^2}\\
&-\left(\nabla_{\boldsymbol{x}}^{\mathrm{sym}}\widetilde{\boldsymbol{w}},2\nu\nabla_{\boldsymbol{x}}^{\mathrm{sym}}\widetilde{\boldsymbol{v}}\right)_{\Omega_0^2}\\
&+\left(\nabla_{\boldsymbol{x}}^{\mathrm{sym}}\widetilde{\boldsymbol{w}},\frac{1}{\rho_1}\boldsymbol{F}\boldsymbol{S}\boldsymbol{F}^T\right)_{\Omega_0^2}\\
&+\left(\widetilde{\boldsymbol{w}},\left(1-\frac{\rho_2}{\rho_1}\right)\boldsymbol{g}\right)_{\Omega_0^2} .
\end{aligned}
\tag{10}
$$

Note that $\widetilde{p}$ and p' have been redefined by dividing through the fluid density ρ_1 as in [14], $\nu=\mu/\rho_1$ is the kinematic viscosity of the fluid, and $\boldsymbol{h}$ is the prescribed traction vector.

2.2. Semi-discrete formulation

In order to perform space discretization, let us start considering a set of NURBS basis functions $\{N_A^{ED}(\boldsymbol{x})\}_{A=1}^{n_{ED}}$ defined over the physical domain Ω. Thanks to the stabilized VMS technique, the same scalar discrete space spanned by the above-mentioned basis functions can be used to represent the weight and trial functions for $\widetilde{p}$ and each Cartesian component of $\widetilde{\boldsymbol{v}}$ without the need to use a stable pressure-velocity combination in the sense of Babŭska and Brezzi [29, 30]. Therefore, we define

$$
\boldsymbol{v}^h(\boldsymbol{x},t)=\sum_{A=1}^{n_{ED}}\boldsymbol{v}_A(t)N_A^{ED}(\boldsymbol{x});\quad p^h(\boldsymbol{x},t)=\sum_{A=1}^{n_{ED}}p_A(t)N_A^{ED}(\boldsymbol{x});
\tag{11}
$$

$$
\boldsymbol{w}^h(\boldsymbol{x})=\sum_{A=1}^{n_{ED}}\boldsymbol{w}_A N_A^{ED}(\boldsymbol{x});\quad q^h(\boldsymbol{x})=\sum_{A=1}^{n_{ED}}q_A N_A^{ED}(\boldsymbol{x}) .
\tag{12}
$$

Analogously, let us consider a set of NURBS basis functions $\{N_B^{LD}(\boldsymbol{X})\}_{B=1}^{n_{LD}}$ defined over the reference domain Ω_0^2. The scalar discrete space spanned by these basis functions will be used to represent the trial functions for each Cartesian component of the displacement

$$
\boldsymbol{u}_2^h(\boldsymbol{X},t)=\sum_{B=1}^{n_{LD}}\boldsymbol{u}_B(t)N_B^{LD}(\boldsymbol{X}) .
\tag{13}
$$

Eq. (3) will also be discretized using the space spanned by $\{N_B^{LD}(\boldsymbol{X})\}_{B=1}^{n_{LD}}$. Since we discretize this equation using collocation, we just need to define a set of collocation points. We will follow the standard practice in IGA and use Greville points (denoted by $\{\boldsymbol{\tau}_i\}_{i=1}^{n_{LD}}$) as our collocation sites. We note, however, that a new set of points referred to as Cauchy-Galerkin points has been recently proposed [31]. Cauchy-Galerkin points have the potential to render the Galerkin solution exactly with a computational cost of one evaluation of the basis functions per degree of freedom.

We will use the isoparametric concept in order to build computational meshes in Ω and Ω_0^2. These meshes will be called Eulerian mesh and Lagrangian mesh, respectively. The Lagrangian mesh can be pushed forward to physical space using the discrete mapping $\boldsymbol{\varphi}^h(\boldsymbol{X}, t)$. This mesh moves on top of the Eulerian mesh in a nonconforming fashion.

To finish the spatial discretization, we express the fine-scale velocity and fine-scale pressure in terms of their coarse-scale counterparts as

$$\boldsymbol{v}' = -\tau_M \left(\frac{\partial \boldsymbol{v}^h}{\partial t} + \boldsymbol{v}^h \cdot \nabla_{\boldsymbol{x}} \boldsymbol{v}^h + \nabla_{\boldsymbol{x}} p^h - \nu \Delta_{\boldsymbol{x}} \boldsymbol{v}^h - \boldsymbol{g} \right) \ , \tag{14}$$

$$p' = -\tau_C \nabla_{\boldsymbol{x}} \cdot \boldsymbol{v}^h \ , \tag{15}$$

where τ_M and τ_C are the stabilization parameters defined as in [32], viz.,

$$\tau_M = \left(s^h(\boldsymbol{x}, t) \left(\frac{4}{\Delta t^2} + \boldsymbol{v}^h \cdot \boldsymbol{G} \boldsymbol{v}^h + C_I \nu^2 \boldsymbol{G} : \boldsymbol{G} \right) \right)^{-\frac{1}{2}} \ , \tag{16}$$

$$\tau_C = \left(\tau_M \mathrm{tr} \boldsymbol{G} \right)^{-1} \ . \tag{17}$$

Here, $\mathrm{tr}(\cdot)$ is the trace operator, $\boldsymbol{G} = [G_{ij}] = \sum_{k=1}^{3} \frac{\partial \xi_k}{\partial x_i} \frac{\partial \xi_k}{\partial x_j}$, $\boldsymbol{x}(\boldsymbol{\xi})$ is the geometrical mapping of the Eulerian mesh, and C_I is a positive constant. Following [33], we take $C_I = 36$ in our simulations.

The scalar function $s^h(\boldsymbol{x}, t)$ that appears in Eq. (16) is a dimensionless scaling factor introduced in the context of immersed FSI methods in [32]. To the best of our knowledge, all available immersed FSI methods assume the pressure field to be continuous across the fluid-solid interface. However, the exact solution to the problem may have discontinuous pressure at the interface. Therefore, the discrete pressure spaces of immersed FSI methods have poor approximation properties at the interface leading to lack of local mass conservation in this region for practical levels of refinement. This issue is particularly notorious for thin solids where solutions with large pressure jumps at the interface are common. As in [32, 34, 35], the above-mentioned scaling factor is introduced to locally weaken the influence of the poorly approximated pressure gradient in Eq. (14) and locally enhance the penalization of volume change due to the inverse relation between τ_M and τ_C. The function $s^h(\boldsymbol{x}, t)$ belongs to the discrete space spanned by $\{N_A^{ED}(\boldsymbol{x})\}_{A=1}^{n_{ED}}$, i.e., $s^h(\boldsymbol{x}, t) = \sum_{A=1}^{n_{ED}} s_A(t) N_A^{ED}(\boldsymbol{x})$. We set the control variables associated with basis functions that intersect the interface to the same value $s_I >> 1$ and the remaining control variables are set to 1.

Finally, the semi-discrete formulation of our immersed method can be stated as: Find $\boldsymbol{v}^h$, p^h, and $\boldsymbol{u}_2^h$ such that, for all $\boldsymbol{w}^h$ and q^h defined as in Eq. (12) and all $\{\boldsymbol{\tau}_i\}_{i=1}^{n_{LD}}$,

$$B^{ED}\left(\{\boldsymbol{w}^h, q^h\}, \{\boldsymbol{v}^h + \boldsymbol{v}', p^h + p'\} \right) - L^{ED}\left(\boldsymbol{w}^h \right) + B^{LD}\left(\boldsymbol{w}^h, \boldsymbol{v}^h; \boldsymbol{u}_2^h \right) = 0 \ , \tag{18}$$

$$\frac{\partial \boldsymbol{u}_2^h}{\partial t}(\boldsymbol{\tau}_i, t) = \boldsymbol{v}^h(\boldsymbol{\varphi}^h(\boldsymbol{\tau}_i, t), t) \ . \tag{19}$$

Remark 1:

The integrals of Eq. (10) demand special attention. Gaussian quadrature rules defined on the elements of the Lagrangian mesh are used to compute those integrals. However, there are functions in the integrands, namely, the weighting functions $\boldsymbol{w}^h$, the coarse-scale velocity $\boldsymbol{v}^h$, and their first derivatives, which are defined on the Eulerian mesh instead of the Lagrangian mesh. Therefore, for a certain Gauss point with parametric coordinates $\boldsymbol{\xi}_G^{LD}$ in the Lagrangian mesh, we first need to compute its physical location $\boldsymbol{x}_G$ using the geometrical mapping of the Lagrangian mesh, i.e, $\boldsymbol{\varphi}^h$. Then, we have to invert the geometrical mapping of the Eulerian mesh in order to obtain the parametric coordinates $\boldsymbol{\xi}_G^{ED}$ associated with the physical point $\boldsymbol{x}_G$ in the Eulerian mesh. Once we know $\boldsymbol{\xi}_G^{ED}$, we can evaluate functions that are defined on the Eulerian mesh using standard procedures of finite elements. Note that an analogous situation occurs when we try to evaluate Eq. (19) at a certain collocation point.

Remark 2:

The above-explained integration process used for B^{LD} is suboptimal because the functions that are defined on the Eulerian mesh may have lines of reduced continuity in the interior of the integration regions which are the elements of the Lagrangian mesh. However, the higher inter-element continuity of spline functions is used in order to alleviate this issue.

Remark 3:

As reported in the literature [36, 37], when piecewise linear Lagrange polynomials are used in immersed FSI, the element size of the Lagrangian mesh is required to be at least twice as small as the element size of the Eulerian mesh in order to achieve stable solutions. Our numerical findings reveal that the use of higher order splines permits to obtain stable solutions utilizing the same element size in both meshes.

2.3. Time discretization and FSI solution strategy

We discretize the first order time derivatives that appear in our immersed FSI formulation using the Generalized-α technique [38], which is an implicit and second-order accurate method with control over the dissipation of high-frequency modes. Once the time discretization has been sorted, we are left with a system of nonlinear algebraic equations that relates the unknown control variables of the Eulerian velocity, Eulerian pressure, and Lagrangian displacement at time t^{n+1} to the known control variables at time t^n. In order to compute the unknown control variables at time t^{n+1}, we derive two separate tangent matrices. One tangent matrix for the linear momentum and mass conservation residuals ($\boldsymbol{R}_{MC}$) where the Lagrangian control variables ($\boldsymbol{U}_{LD}$) are considered to be constant and another tangent matrix for the kinematic equation residual ($\boldsymbol{R}_K$) where the Eulerian control variables ($\boldsymbol{U}_{ED}$) are considered to be constant. The tangent matrix associated to $\boldsymbol{R}_K$ is computed by linearizing the residual with respect to the physical values of the Lagrangian displacements at collocation points. The reason is that this tangent matrix is much sparser than that obtained by linearizing with respect to the control variables. Actually, by using

the advocated tangent matrix we only need to solve an independent $d \times d$ linear system for each collocation point. Furthermore, we apply the so-called block-iterative approach for solving these two subproblems [39, 40]. This fully-implicit approach boils down to finding a root of the residuals $\boldsymbol{R}_{MC}$ and $\boldsymbol{R}_K$ given initial guesses for $\boldsymbol{U}_{ED}$ and $\boldsymbol{U}_{LD}$ following the next steps:

1. Compute the residual $\boldsymbol{R}_K$ by evaluating Eq. (19) at each collocation point and the corresponding tangent matrix by linearizing with respect to the physical values of the displacements at collocation points.
2. Solve a $d \times d$ linear system for each collocation point where the unknowns are the physical values of the displacement at the collocation point.
3. Compute the Lagrangian control variables from the displacement physical values at the collocation points. This is done collocating Eq. (13) and solving a linear system. Note that the matrix of this linear system depends only on the parametric configuration of the Lagrangian mesh. Therefore, we just need to compute the matrix once, store it, and use it in each Newton-Raphson iteration of each time step. This finalizes the update of the Lagrangian control variables $\boldsymbol{U}_{LD}$.
4. Assemble the residual $\boldsymbol{R}_{MC}$. We recall that the assembly of $\boldsymbol{R}_{MC}$ is not standard since it requires to go from the parametric coordinates of a quadrature point in the Lagrangian mesh to its associated parametric point in the Eulerian mesh at the proper time level. This process was explained in detail in [24] and avoids errors associated with either interpolating or projecting functions from the Eulerian mesh to the Lagrangian mesh.
5. Assemble an approximate tangent matrix $\boldsymbol{K}_{MC} \simeq \dfrac{\partial \boldsymbol{R}_{MC}}{\partial \boldsymbol{U}_{ED}}$. We are using the approximation to the tangent matrix given in [14].
6. Solve the linear system $\boldsymbol{K}_{MC} \Delta \boldsymbol{U}_{ED} = -\boldsymbol{R}_{MC}$.
7. Update the Eulerian control variables $\boldsymbol{U}_{ED} \leftarrow \boldsymbol{U}_{ED} + \Delta \boldsymbol{U}_{ED}$.

This process is repeated until each component of $\boldsymbol{R}_{MC}$ and $\boldsymbol{R}_K$ is sufficiently converged. In particular, in all the simulations performed in this paper, we stop the iterative process when the L^2-norm of each residual component has decreased more than four orders of magnitude. To linearize the residual $\boldsymbol{R}_{MC}$, we use a Newton-Raphson algorithm with line search [41]. Regarding the linear solver for Step 6, we use the generalized minimum residual method (GMRES) [42, 43] with relative tolerance set to 10^{-5}. The use of the function s^h in Eq. (16) increases the condition number of $\boldsymbol{K}_{MC}$ for large values of the parameter s_I. This makes it quite challenging to find a suitable preconditioner. Our implementation is built on top of PetIGA [44, 45, 46], which gives us direct access to the preconditioners of the scientific librery PETSc [47, 48]. For parallel MPI simulations with a relatively low number of processors (up to 32 or 64 cores depending on the size of the problem), the best performance is given by the restricted additive Schwarz preconditioner with the following options: LU decomposition as subdomain solver, one subdomain per processor, and nested dissection as matrix reordering technique so as to reduce the ratio of fill-ins

and enhance the stability of the LU decomposition. However, for parallel MPI simulations with a larger number of processors (we have tried up to 256 cores), the best performance is given by the block Jacobi preconditioner with the following options: LU decomposition as subdomain solver, two subdomains per processor so as to enhance the communication between subdomains [49], and nested dissection as matrix reordering method.

Remark 4:

In various of the simulations presented in the following Sections, we will have several solids embedded in the domain Ω. The aforementioned block-iterative technique is highly efficient since we just have to repeat Steps 1, 2, and 3 for each solid and assemble its contribution to $\boldsymbol{R}_{MC}$ in Step 4.

3. Numerical simulations of capsules and compound capsules in shear flow

The velocity field of a linear shear flow in the x direction has the form $\boldsymbol{v}_{shear} = (\dot{\gamma}z, 0, 0)$ where $\dot{\gamma}$ is the constant shear rate that characterizes the flow's strength. For low Reynolds numbers, shear flows can be produced in rectangular and parallelogram geometries by setting velocity boundary conditions compatible with $\boldsymbol{v}_{shear}$ and letting the Navier-Stokes equations evolve in time. In this Section, we follow a similar approach, but we embed capsules and compound capsules in the flow. The goal is to study their motions and how they modify the velocity field.

3.1. Qualitative description of the motion of a capsule

A capsule, which is used as our RBC mimic, is composed by a very thin membrane with a fluid inside. From theoretical and experimental developments, it is known that the following dimensionless numbers control the dynamics of an individual capsule to a significant extent:

- The swelling degree of the membrane (Δ_m). In a three-dimensional setting, the swelling degree is defined as the ratio of the volume enclosed by the membrane (V_e) to the volume of a sphere with the membrane external area (A_c), that is, $\Delta_m = 6\sqrt{\pi}V_e/\sqrt{A_c^3}$. Its two-dimensional counterpart is defined as the ratio of the area enclosed by the membrane (A_e) to the area of a circle with the membrane perimeter (P_c), that is, $\Delta_m = 4\pi A_e/P_c^2$.

- The confinement degree (χ). This quantity is the ratio of the effective membrane radius (R_0) to the channel half-width. In a three-dimensional setting, R_0 is defined as the radius of a sphere with the membrane external area, i.e., $R_0 = \sqrt{A_c/4\pi}$. Analogously, in a two-dimensional setting, R_0 is the radius of a circle with the membrane perimeter, i.e., $R_0 = P_c/2\pi$[†].

[†]Some authors define an effective radius over the volume/area enclosed by the membrane in a three-/two-dimensional setting, respectively.

- The viscosity contrast (Λ). The membrane encloses an internal fluid of viscosity μ_i and it is suspended in an outer fluid of viscosity μ_o, thus defining the viscosity contrast as $\Lambda = \mu_i/\mu_o$. In this paper, we consider internal and outer fluids with the same viscosity μ, therefore, $\Lambda = 1$.

- The surface capillary number of the membrane (C_a^m). The parameter C_a^m quantifies the relative strength of the viscous forces exerted by the external fluid to the elastic forces exerted by the membrane. Its precise form is given by $C_a^m = \mu_o \dot{\gamma} R_0/hG_m$, where $\dot{\gamma}$ is the average shear rate, h is the membrane thickness, and G_m is the membrane shear modulus.

- The Reynolds number (R_e). The parameter R_e quantifies the relative strength of the inertial forces to the viscous forces exerted by the external fluid. The relevant Reynolds number for this problem is $R_e = \rho_1 \dot{\gamma} R_0^2/\mu_o$.

A single capsule in shear flow exhibits two main types of motion, viz., tank-treading and tumbling. These two motions were first observed in experiments with RBCs in shear flow in [50, 51, 52]. In the tank-treading (TT) motion, the RBC membrane adopts a nearly constant orientation with the flow direction and rotates around the hemoglobin like the tread of a tank. The two main physical quantities that characterize a TT motion are the inclination angle of the membrane with the flow direction (θ) and the frequency of the TT motion (ω_{TT}). In the tumbling (TU) motion, the RBC rotates as a whole around its center of gravity. The main physical quantity that characterizes a TU motion is its frequency (ω_{TU}). For capsules, the transition from TT to TU is mainly determined by the viscosity contrast. For $\Lambda = 1$, TT motion is expected. In this paper, we will represent capsules using solid-shell NURBS elements, although the use of fully nonlinear Kirchhoff-Love shells [53, 54] may be a good alternative taking into account the small thickness of capsules.

3.2. Qualitative description of the motion of a compound capsule

A compound capsule, which is proposed here as a CTC mimic, is composed by a very thin membrane, an inclusion (i.e., a bulky solid) and a fluid between the membrane and the inclusion. The dynamics of a compound capsule are controlled by the quantities described in Section 3.1. and the following dimensionless numbers:

- The filling fraction (ϕ). In a three-dimensional setting, ϕ is the ratio of the inclusion volume to the volume enclosed by the membrane. Its two-dimensional counterpart is defined as the ratio of the inclusion area to the area enclosed by the membrane.

- The swelling degree of the inclusion (Δ_i). The definition of Δ_i is analogous to that of Δ_m.

- The bulk capillary number of the inclusion (C_a^i). The quantity C_a^i measures the relative strength of the viscous forces exerted by the internal fluid to the elastic forces exerted by the inclusion. It is defined as $C_a^i = \mu_i \dot{\gamma}/G_i$, where G_i is the inclusion shear modulus.

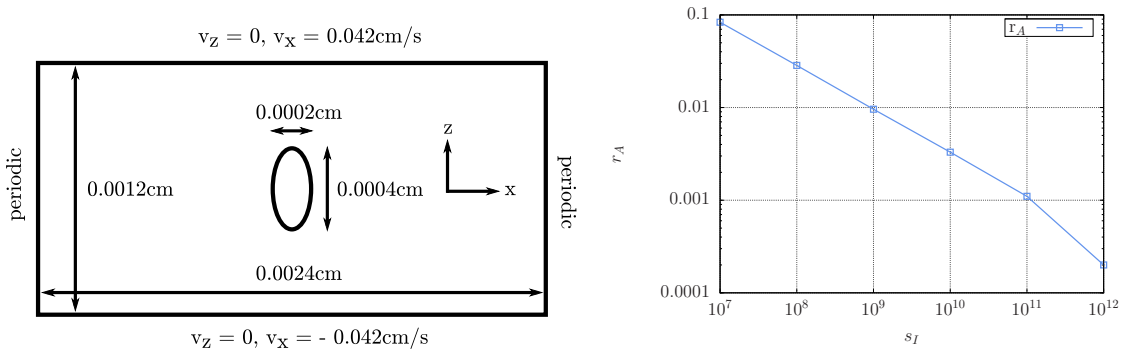

(a) Problem setup (b) Relative area change

Figure 1: Parameter sweep of s_I to asses mass conservation errors near the fluid-solid interface. a) Geometrical description of the considered problem together with the boundary conditions applied. b) Relative area change of an elliptic capsule in shear flow at $t = 1.0$ s with $\Delta t = 0.0005$ s.

The numerical simulations that follow are aimed at gaining a deeper understanding of the dynamics of a compound capsule in shear flow.

3.3. Adjusting s_I so as to enforce the incompressibility constraint at the interface

As explained in Section 2.2 and following [32], we modify the VMS stabilization close to the fluid-solid interface introducing the dimensionless parameter s_I in order to compensate the poor approximation properties of the pressure field in that region. In order to decide a suitable value for s_I, we measure the area change of a two-dimensional capsule for different values of s_I.

The domain Ω is a rectangle of 0.0024×0.0012 cm^2. Periodic boundary conditions are applied in the horizontal direction. We use Dirichlet boundary conditions in the top and bottom walls as indicated in Fig. 1 a). The described boundary conditions lead to a shear rate $\dot{\gamma} = 70$ s^{-1}, which is within the range found in microcirculation [55]. An elliptic capsule is initially placed at the center of the domain with its longer axis perpendicular to the flow direction [see Fig. 1 a)]. The semiaxes of the ellipse are $a = 0.0002$ cm and $b = 0.0001$ cm, which lead to $R_0 = 0.0001542$ cm. The thickness of the membrane is $h = 5 \cdot 10^{-7}$ cm. The remaining physical parameters are taken as follows: $\mu = 0.012$ g/(cm s), $\rho_1 = 1.025$ g/cm^3, $\rho_2 = 1.1$ g/cm^3, $G_m = 7500$ dyn/cm^2, and $\boldsymbol{g} = (0, 0)$. With these parameters, the above-mentioned dimensionless numbers are: $\Delta_m = 0.841$, $\chi = 0.257$, $\Lambda = 1$, $C_a^m = 0.0345$, and $R_e = 0.000142$.

Here and in the remaining simulations of this paper, our solid material model is given by the second Piola-Kirchhoff stress tensor

$$\boldsymbol{S} = GJ^{-2/d}\left(\boldsymbol{I} - \frac{1}{d}\mathrm{tr}(\boldsymbol{C})\boldsymbol{C}^{-1}\right) , \tag{20}$$

where G is the shear modulus and $\boldsymbol{C} = \boldsymbol{F}\boldsymbol{F}^T$ is the Cauchy-Green deformation tensor.

An Eulerian mesh with 256×128 cubic NURBS elements is used to represent the rectangular domain Ω. To represent the capsule we use NURBS basis functions of second order or higher, which, unlike Lagrange polynomials, can represent a hollow ellipse exactly. In this simulation, we use a Lagrangian mesh with 1×208 quadratic NURBS elements. The time step is $\Delta t = 0.0005$ s.

We define the relative area change of the capsule at time t as

$$r_A(t) = \frac{\int_{\Omega_t^2} \mathrm{d}\Omega_t^2 - \int_{\Omega_0^2} \mathrm{d}\Omega_0^2}{\int_{\Omega_0^2} \mathrm{d}\Omega_0^2}. \tag{21}$$

In this simulation, the capsule acquires a nearly constant inclination angle at time $t = 0.15$ s. At time $t = 1$ s, the membrane particles have already completed more than three turns in their TT motion. Fig. 1 b) shows the value of r_A for different values of s_I at time $t = 1$ s. As expected, the spurious area change decreases as we rise the dimensionless parameter s_I. As we increase the value of s_I, the number of linear iterations needed per nonlinear iteration increases because the condition number of the tangent matrix becomes greater. However, the number of nonlinear iterations per time step decreases because larger values of s_I render a less stiff residual of the mass conservation equation, which is usually the bottleneck for nonlinear convergence. In particular, for this case, which is solved using the restricted additive Schwarz preconditioner, the computational time was lowest for $s_I = 10^{10}$. Based on Fig. 1 b), we believe that $s_I = 10^{10}$ produces mass conservation errors which are sufficiently small for our target applications. Therefore, we will use this value of s_I in all the simulations of shear flow unless otherwise specified. Consistently with [32], we find that large errors in the incompressibility constraint may even alter the qualitative character of the numerical solutions. For example, for $s_I \leq 10^5$, the capsule no longer undergoes a classical TT motion. To test and validate an immersed FSI algorithm, we recommend to check the errors incurred in the incompressibility constraint near the fluid-solid interface.

Under physiological conditions, both the RBC volume and external area are known to remain nearly constant. We are not enforcing the capsule external area to be constant in our formulation. However, we will measure its time evolution in our simulations. In order to do so, we define the relative perimeter change of the capsule in our two-dimensional setting as

$$r_P(t) = \frac{\int_{\Gamma_t^2} \mathrm{d}\Gamma_t^2 - \int_{\Gamma_0^2} \mathrm{d}\Gamma_0^2}{\int_{\Gamma_0^2} \mathrm{d}\Gamma_0^2}. \tag{22}$$

In the simulations shown in Section 3, the relative perimeter change is always lower than 0.04. We believe that this value is acceptable for the purposes of this paper. There are capsule formulations based on shells that impose the constraint of external area in

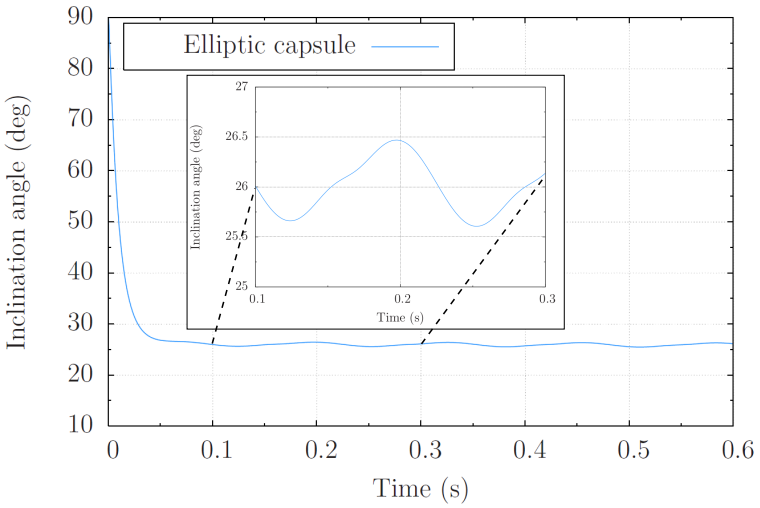

Figure 2: Time evolution of the inclination angle. In this case, there is an oscillation with an amplitude smaller than 1° around the value 26.06°

their formulations [56, 57]. However, as pointed out in [58], when these models are used in immersed FSI, this constraint is usually loosened in order to achieve convergence of the FSI scheme.

3.4. Spatial and temporal resolution study

In this Section, we perform a mesh independence study for the problem stated in Section 3.3. The quantities of interest will be the inclination angle and the TT frequency for different meshes and time steps. In our simulations, the inclination angle is computed as the angle between the minor principal axis of inertia of the capsule and the flow direction. The TT frequency is computed as the average frequency with which the particles of the membrane move.

When the inclination angle of a RBC is experimentally measured, it oscillates between 0.1° and 2° around a certain average value. This oscillation was initially attributed to thermal fluctuations [5]. However, this oscillation was also found in numerical simulations with capsules that do not take into account thermal fluctuations [59, 58, 60] and it is also present in the TT motions shown in this Section; see Fig. 2. To compute the inclination angle, we monitor its time evolution and when it enters an oscillatory regime, we take the mean value.

We consider quadratic and cubic Eulerian meshes and perform h-refinement. In all cases, we define a quadratic Lagrangian mesh with slightly smaller element size than that of the Eulerian mesh under consideration[‡]. The results are shown in Table 1. First of all, the data shows that, for the time steps used, the time integration is not compromising the

[‡]We have also tried cubic Lagrangian meshes, Lagrangian meshes with more than one element in the through-thickness direction, and Lagrangian meshes with element size twice as small as that of the Eulerian mesh (data not shown). Neither θ nor ω_{TT} changed with respect to the results shown in Table 1.

# elements (Eulerian mesh)	Degree (Eulerian mesh)	Δt (s)	θ (°)	ω_{TT} (s^{-1})
96×48	2	0.001	17.81	3.20
96×48	3	0.001	23.95	3.54
128×64	2	0.001	22.14	3.46
128×64	2	0.0005	22.24	3.45
128×64	3	0.001	25.22	3.58
128×64	3	0.0005	25.22	3.58
192×96	2	0.0005	24.45	3.59
192×96	3	0.0005	25.77	3.78
256×128	2	0.0005	25.24	3.72
256×128	2	0.00025	25.24	3.72
256×128	3	0.0005	25.99	3.84
256×128	3	0.00025	25.99	3.84
384×192	2	0.0005	25.80	3.84
384×192	2	0.0001	25.80	3.84
384×192	3	0.0005	26.06	3.88
384×192	3	0.0001	26.06	3.88
512×256	2	0.00025	25.87	3.87
512×256	3	0.00025	26.09	3.90

Table 1: Spatial and temporal resolution study. We analyze the influence of the discretization on the inclination angle and TT frequency.

accuracy of the solution. Second of all, for a given number of elements, cubics are more accurate than quadratics. This was expected due to their higher power of approximation [61, 33]. However, the significant differences observed in the data may be also attributed to the suboptimal integration issue mentioned in Section 2.2, which is alleviated using cubics. Finally, the small differences in θ and ω_{TT} for finer levels of refinement suggest that a converged result has been obtained.

Based on this mesh independence study, we will use an Eulerian mesh with 384×192 cubic elements, a quadratic Lagrangian mesh with a slightly smaller element size than that of the Eulerian mesh, and $\Delta t = 0.0005$ s in all the two-dimensional simulations of Section 3.5 and Section 3.6.

3.5. Dynamics of a capsule

We consider capsules with different geometries and embed them in the shear flow defined in Section 3.3. We start working with six elliptic capsules with different swelling degrees. In order to create these capsules, we vary the longer semiaxis of the capsule defined in Section 3.3 and keep unchanged all the other geometrical and mechanical parameters of the capsule. We consider the following values for a: 0.0001 cm, 0.0002 cm, 0.0003 cm, 0.0004 cm, 0.0005 cm, and 0.00055 cm. The computed inclination angle and TT frequency for each capsule are plotted in Fig. 3 a) and b), respectively. Consistently with the results reported in [62], both θ and ω_{TT} increase with the value of the swelling degree.

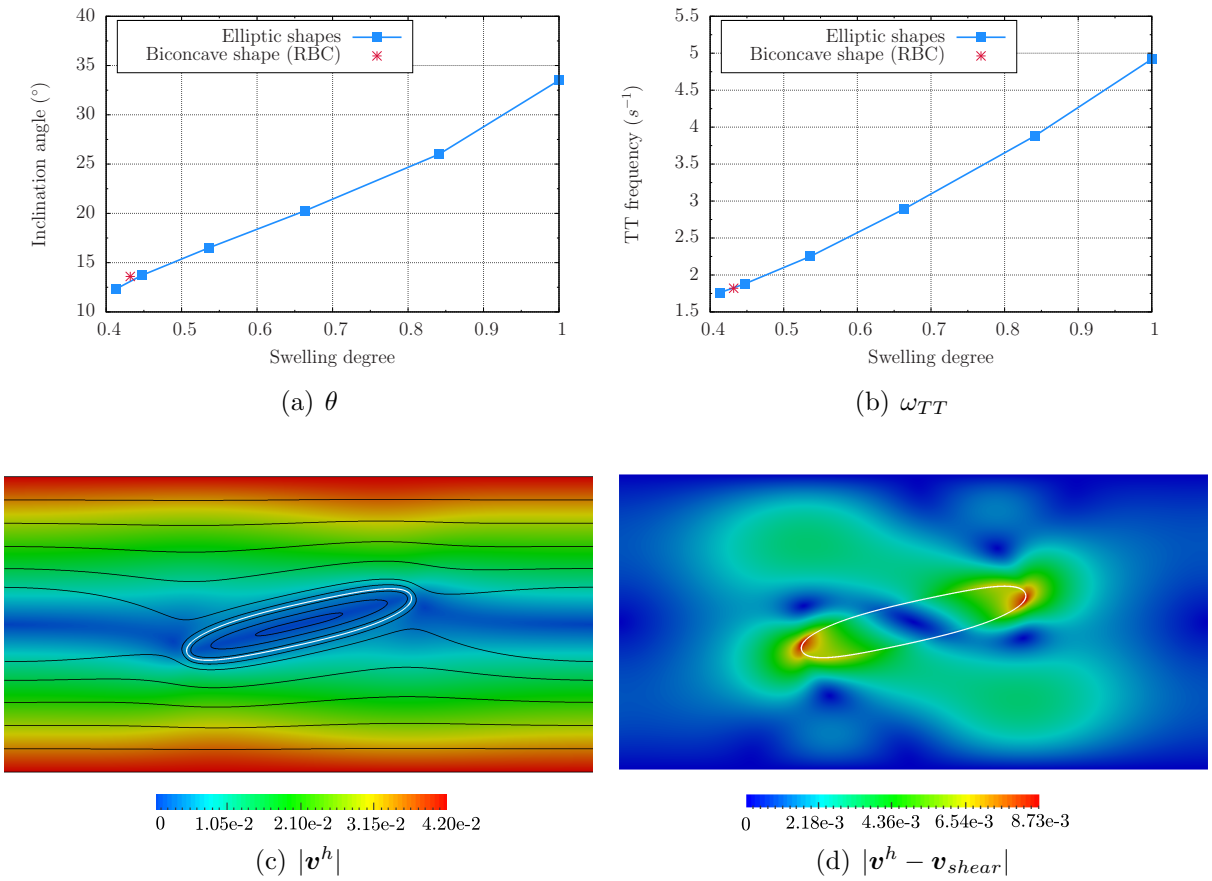

(a) θ (b) ω_{TT}

(c) $|\boldsymbol{v}^h|$ (d) $|\boldsymbol{v}^h - \boldsymbol{v}_{shear}|$

Figure 3: Capsules with different shapes under shear flow. (a) Inclination angle of a capsule as a function of the swelling degree. (b) Tank-treading frequency of a capsule as a function of the swelling degree. (c) Velocity magnitude along with the flow streamlines at time $t = 0.5$ s for the capsule with initial biconcave shape. The black lines represent the streamlines and the white line denotes the capsule. There is a vortex whose center is located at the center of gravity of the capsule. (d) Perturbations introduced by the biconcave capsule with respect to the shear component at time $t = 0.5$ s.

Now, we repeat the analysis considering a capsule with the biconcave shape that RBCs have in a quiescent fluid, which is defined in [57]. The computed θ and ω_{TT} for this new initial shape are plotted in Figs. 3 a) and b) with a red star. The results suggest that the swelling degree characterizes quite accurately the behavior of capsules in the nonlinear regime independently of their initial shape.

Fig. 3 c) displays a contour plot of the velocity magnitude ($|\boldsymbol{v}^h|$) with flow streamlines for the biconcave shape at time $t = 0.5$ s. The streamlines close to the capsule are parallel to the membrane which is a consequence of its tank-treading motion. Fig. 3 d) plots the velocity field resulting from our FSI simulation minus the shear component ($|\boldsymbol{v}^h - \boldsymbol{v}_{shear}|$) in order to show how the presence of the capsule modifies the flow conditions.

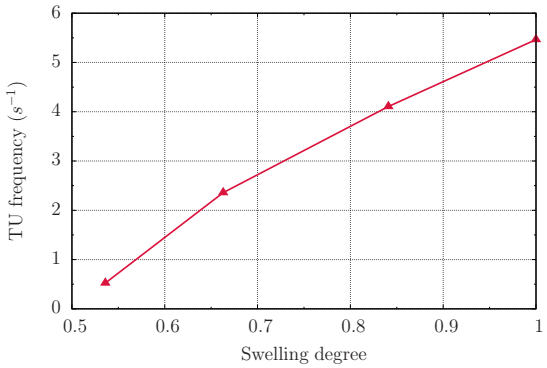

(a) ω_{TU} of bulky solids

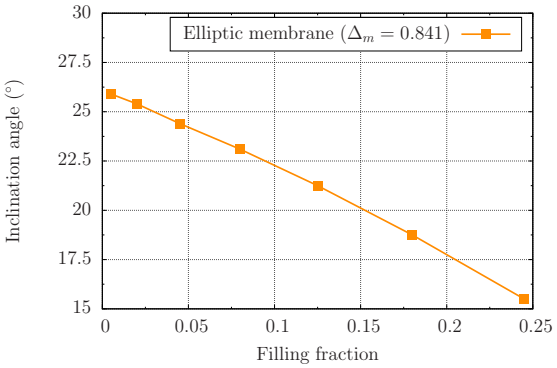

(b) θ of the membrane (compound capsule)

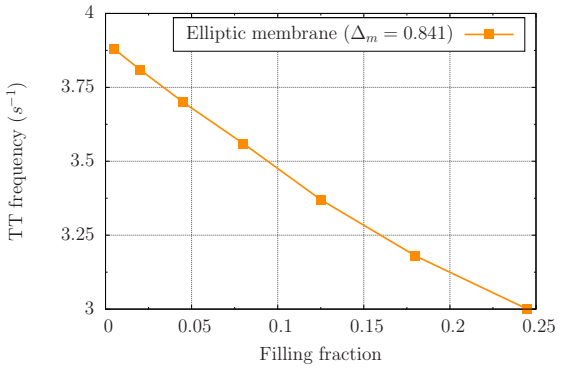

(c) ω_{TT} of the membrane (compound capsule)

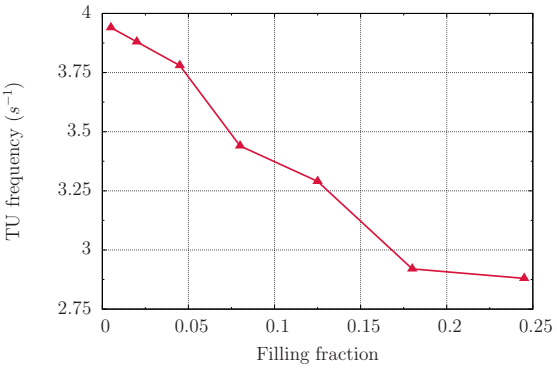

(d) ω_{TU} of the inclusion (compound capsule)

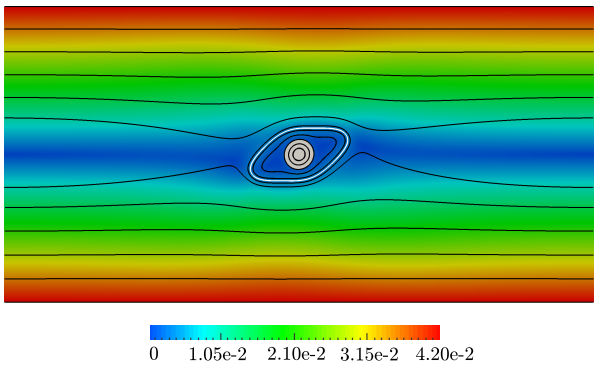

(e) $|\boldsymbol{v}^h|$

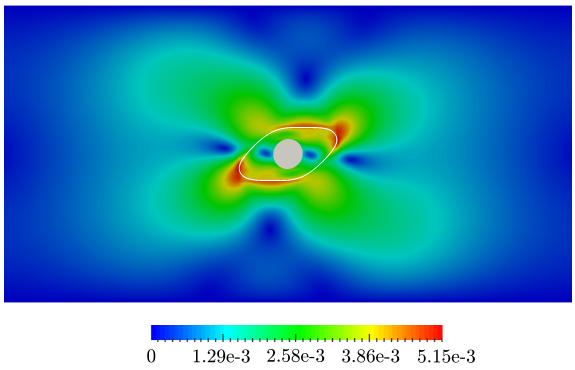

(f) $|\boldsymbol{v}^h - \boldsymbol{v}_{shear}|$

Figure 4: Bulky solids and compound capsules under shear flow. (a) Tumbling frequency of a bulky solid under shear flow as a function of the swelling degree. (b) Inclination angle of the membrane of a compound capsule as a function of the filling fraction. (c) Tank-treading frequency of a compound capsule membrane as a function of the filling fraction. (d) Tumbling frequency of an inclusion under pure shear flow as a function of the filling fraction. (e) Velocity magnitude along with the flow streamlines at time $t = 0.5$ s for the compound capsule with $\phi = 0.180$. The streamlines near the boundary of the compound capsule are parallel to the membrane due to its tank-treading motion. (f) Perturbations introduced by the compound capsule with respect to the shear component at time $t = 0.5$ s for the compound capsule with $\phi = 0.180$.

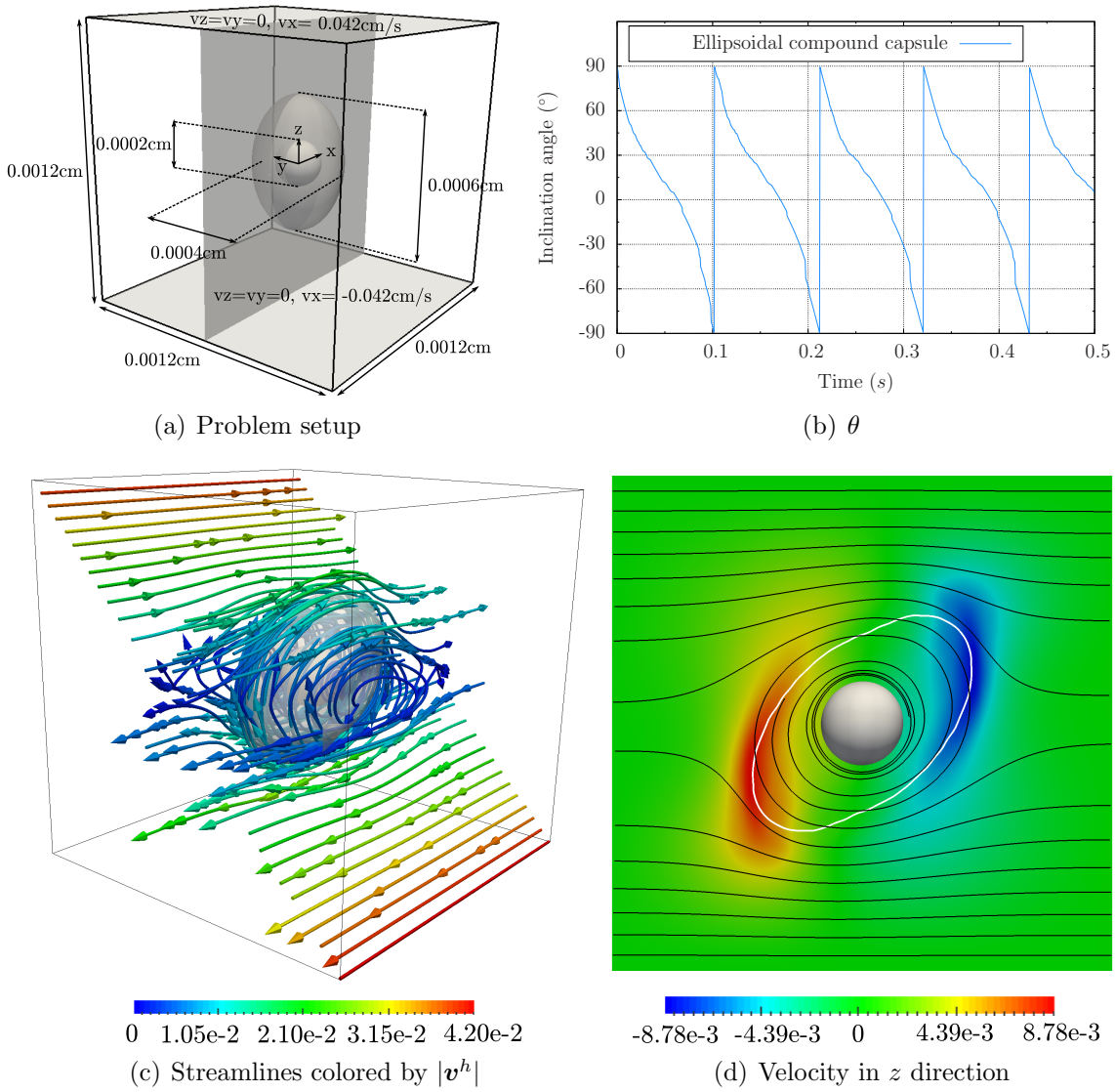

(a) Problem setup

(b) θ

(c) Streamlines colored by $|\boldsymbol{v}^h|$

(d) Velocity in z direction

Figure 5: A compound capsule undergoing a TU motion in a three-dimensional setting. (a) Geometrical description of the problem along with Dirichlet boundary conditions applied on the two shaded faces of the cube. Periodic boundary conditions are applied in the other four faces. The shaded plane, i.e., the plane $y = 0$ is used to plot the z component of the velocity in Fig. 5 d). (b) Time evolution of the inclination angle. (c) Streamlines colored by the velocity magnitude at time $t = 0.23$ s. A transparent membrane is plotted in order to see the streamlines and the inclusion inside of it. The boundary of Ω is represented by black lines. (d) Velocity in z direction on the plane indicated in Fig. 5 a) at time $t = 0.23$ s along with the streamlines.

3.6. Dynamics of a compound capsule

Cells with nucleus, e.g., WBCs, have been often modeled as bulky solids [63] or fluid-filled membranes [64, 65]. However, these models fail to accurately reproduce the basic dynamics of nucleated cells [66]. For example, we have embedded bulky ellipses with

different swelling degrees in the shear flow defined in Section 3.3. As expected, they all perform a TU motion whose frequency is plotted in Fig. 4 a). However, one may foresee more complicated types of motion for a cell with nucleus. For this reason, alternative models have recently been proposed such as bilamellar vesicles [67] and compound vesicles [16], which aim at capturing the internal structure of these cells more accurately by mimicking the effect of the nucleus. In this work, we present compound capsules as the capsule counterpart of the model introduced in [16][§].

We start embedding compound capsules formed by circular inclusions ($\Delta_i = 1$) of different sizes. We consider the following values for the inclusion radius r: 0.00001 cm, 0.00002 cm, 0.00003 cm, 0.00004 cm, 0.00005 cm, 0.00006 cm, and 0.00007 cm. The shear modulus of the inclusion is $G_i = 40$ dyn/cm^2, hence $C_a^i = 0.021$. In all cases, we consider the elliptic membrane defined in Section 3.3, which leads to compound capsules with different filling fractions. In these simulations, the membrane undergoes a TT motion while the inclusion performs a TU motion. The values of θ and ω_{TT} for the membrane are plotted for each compound capsule in Fig. 4 b) and c), respectively. Consistently with [16], both the inclination angle and the TT frequency decrease with the filling fraction value. Moreover, the inclination angle and TT frequency values tend to those of a capsule as the inclusion becomes smaller, which can be seen comparing Fig. 4 with Fig. 3. The TU frequency of the inclusion is plotted in Fig. 4 d). Fig. 4 e) displays a contour plot of the velocity magnitude with the flow streamlines at time $t = 0.5$ s for the case $\phi = 0.180$. Fig. 4 f) plots $|\boldsymbol{v}^h - \boldsymbol{v}_{shear}|$ at time $t = 0.5$ s.

Finally, we consider a compound capsule in a three-dimensional setting; see 5 a). The domain Ω is a cube of side 0.0012cm. Periodic boundary conditions are applied in the two horizontal directions and Dirichlet boundary conditions are applied in the top and bottom walls so as to impose a pure shear flow with shear rate $\dot{\gamma} = 70$ s^{-1}. We embedded a compound capsule at the center of the cube. The membrane is an ellipsoid with semiaxes $a = 0.0003$ cm, $b = 0.0002$ cm, and $c = 0.0002$ cm which is initially oriented as in Fig. 5 a). The thickness of the membrane is $h = 5 \cdot 10^{-7}$ cm and its effective radius is $R_0 = 0.000232$ cm. The inclusion is a sphere with a radius $r = 0.0001$ cm. The remaining physical parameters are taken as follows: $\mu = 0.012$ g/(cms), $\rho_1 = 1.025$ g/cm^3, $\rho_2 = 1.1$ g/cm^3, $G_m = 7500$ dyn/cm^2, $G_i = 40$ dyn/cm^2. With these parameters, the dimensionless numbers are: $\Delta_m = 0.960$, $\Delta_i = 1.0$, $\chi = 0.387$, $\Lambda = 1$, $C_a^m = 0.0520$, $Re = 0.000322$, $C_a^i = 0.021$, and $\phi = 0.083$.

An Eulerian mesh with 262144 quadratic NURBS elements is used to represent the cube. To represent the solid, we use NURBS functions of second order, which are able to represent exactly both a hollow ellipsoid and a bulky sphere. We use meshes with 3072 (ellipsoid) and 7168 (sphere) quadratic NURBS elements. This problem is solved using the block Jacobi preconditioner and s_I was set to 10^9. In this computation, both the membrane and the inclusion perform a TU motion, i.e., the two of them rotate as a whole around

[§]The term compound capsule was recently used in [68]. However, following the terminology of [16, 67], the authors do not use compound capsules, but bilamellar capsules, i.e., a capsule inside another capsule.

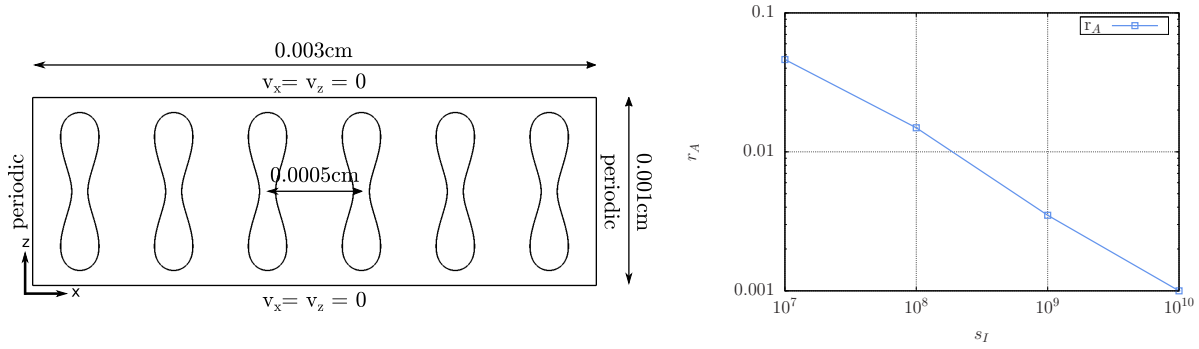

(a) Problem setup

(b) Relative area change

Figure 6: Parameter sweep of s_I. This study verifies that the mass conservation equation is adequately enforced near the fluid-solid interface. a) Geometrical description of the considered problem together with the boundary conditions imposed. b) Relative area change of RBCs in parabolic flow at $t = 1.1$ s with $\Delta t = 0.00025$ s.

their center of gravity. A TU motion is characterized by its average frequency which in this case is 4.68 s^{-1} for both the inclusion and the membrane. In Fig. 5 b), we show how the inclination angle varies in time. Fig. 5 c) displays the streamlines colored by the velocity magnitude in a diagonal plane of the cube and close to the compound capsule at time $t = 0.23$ s. Fig. 5 d) displays the z component of the velocity on the plane indicated in Fig. 5 a). This component is responsible for the TU motion of the membrane.

4. Numerical simulations of capsules and compound capsules in parabolic flow

In this Section, we study the behavior of our cell mimics in flows driven by a pressure gradient. For low Reynolds numbers and in the absence of solids this produces parabolic flows. We study how the flow is modified by capsules and compound capsules and the motions undergone by our cell mimics.

4.1. Adjusting s_I so as to enforce the incompressibility constraint at the interface

We start deciding a suitable value of s_I. Finding an adequate value of s_I is, in principle, a problem-dependent task and it should be done for each type of problem.

The domain Ω is the rectangle of 0.003×0.001 cm^2 shown in Fig. 6 a). Periodic boundary conditions are applied in the horizontal direction and no-slip boundary conditions are applied in the top and bottom walls. The pressure gradient is applied as a body force defined by $\boldsymbol{g} = (1666.66 \text{ dyn/cm}^3, 0 \text{ dyn/cm}^3)$. This leads to velocities that are within the range found in microcirculation [55]. Six capsules with the RBC shape defined in [57] are evenly distributed in the horizontal direction with its long side perpendicular to the flow direction as shown in Fig. 6 a). The thickness of the RBC is $h = 5 \cdot 10^{-7}$ cm. The remaining physical parameters are taken as follows: $\mu = 0.012$ g/(cms), $\rho_1 = 1.025$ g/cm^3, $\rho_2 = 1.1$ g/cm^3, and $G_m = 7500$ dyn/cm^2.

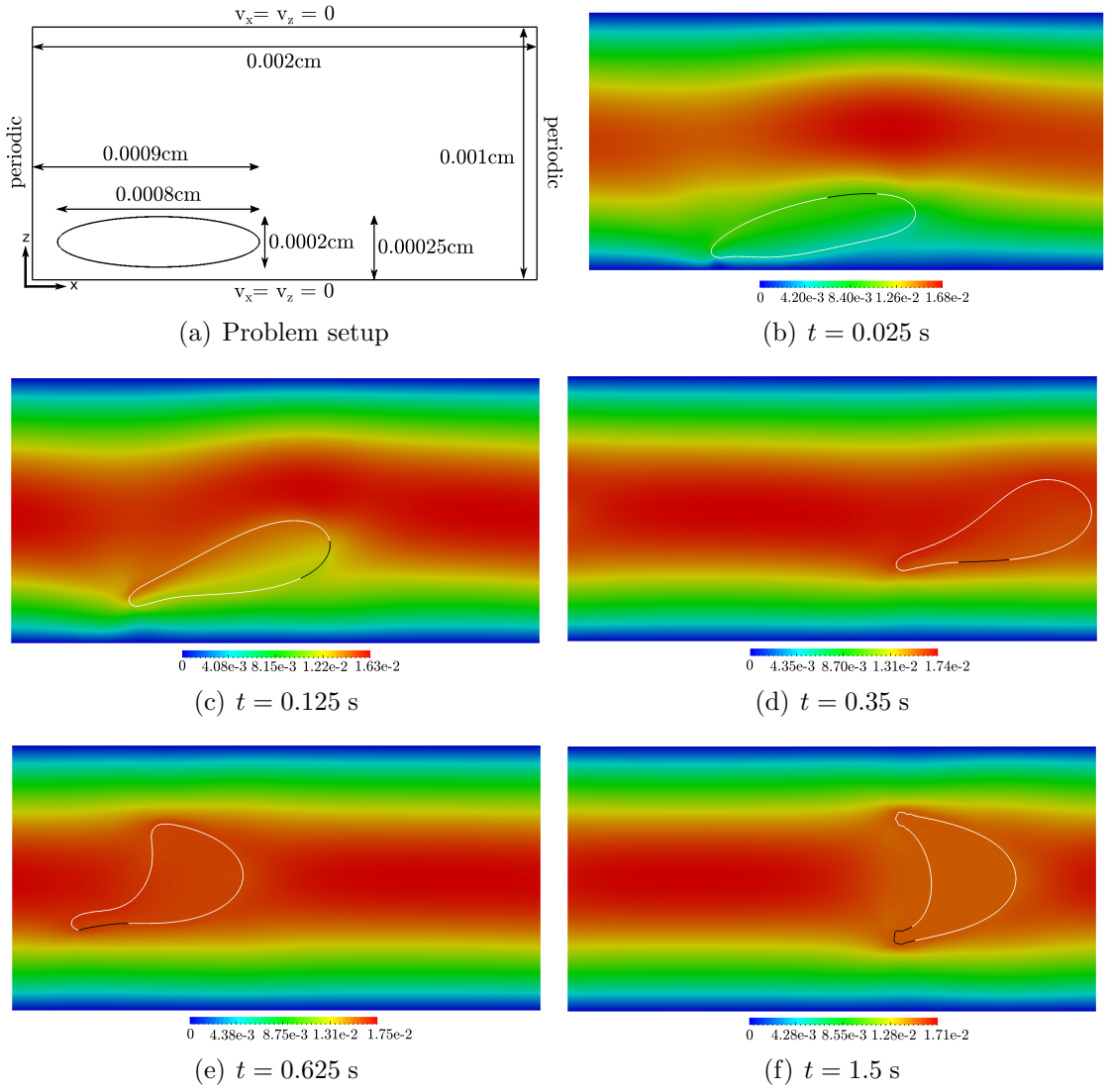

(a) Problem setup (b) $t = 0.025$ s

(c) $t = 0.125$ s (d) $t = 0.35$ s

(e) $t = 0.625$ s (f) $t = 1.5$ s

Figure 7: Capsule in parabolic flow. a) Geometrical description of the problem together with the boundary conditions applied. b)-f) Snapshots describing the lateral migration of the capsule induced by the variation in the shear rate. The capsule undergoes a transitory tank-treading motion until it gets its final parachute-like symmetric shape shown in f). A small portion of the membrane is colored in black so that the TT motion can be observed.

An Eulerian mesh with 384×128 cubic NURBS elements is used to represent the rectangle. A Lagrangian mesh with 1×328 quadratic NURBS elements is used to represent each RBC. The time step used in the computation is $\Delta t = 0.00025$ s.

In this simulation, RBCs acquire a nearly constant shape at time $t = 0.45$ s. By time $t = 1.1$ s, the cells have already looped twice the periodic domain. Fig. 6 b) plots the value of r_A for different values of s_I at time $t = 1.1$ s. As in Section 3.3, the spurious area change decreases as we rise the dimensionless parameter s_I. Again, the number of linear iterations per nonlinear step increases with the value of s_I, but the number of nonlinear iterations per time step decreases with the value of s_I. In this case, the computational time was lowest for $s_I = 10^8$. However, we will use the value $s_I = 10^9$ in the remaining simulations of this Section to have a more accurate result.

In the simulations shown in Section 4, the relative perimeter change was always lower than 0.03. This implies that in this aspect, the results are even better than in the previous Section.

4.2. Dynamics of a capsule

In this Section, we consider an off-center capsule and study its motion and shape evolution. The domain is the rectangle of 0.002×0.001 cm^2 drawn in Fig. 7 a), which is discretized using an Eulerian mesh with 256×128 cubic NURBS elements. The geometry of the capsule is a hollow ellipse with thickness $h = 5 \cdot 10^{-7}$ cm and semiaxes $a = 0.0002$ cm and $b = 0.0001$ cm. The initial position of the capsule is indicated in Fig. 7 a). The capsule is discretized using a Lagrangian mesh with 1×360 quadratic elements. The remaining physical parameters are the following: $\mu = 0.012$ g/(cm s), $\rho_1 = 1.025$ g/cm^3, $\boldsymbol{g} = (1666.66$ dyn/cm$^3, 0$ dyn/cm$^3)$, $\rho_2 = 1.1$ g/cm^3, and $G_m = 7500$ dyn/cm^2. The time step is $\Delta t = 0.00025$ s.

In a flow driven by a pressure gradient, vesicles and RBCs undergo a lateral migration towards the central region of the tube where the shear rate is minimal [69, 70, 71]. Figs. 7 b) to 7 f) describe this migration process for the considered capsule. During the lateral migration, the capsule varies its shape from a hollow ellipse to a parachute-like shape, which is often acquired by RBCs in small tubes [71]. Finally, we would like to mention that the membrane undergoes a tank-treading motion while the solution to the problem is non-symmetric. A small piece of the membrane is colored in black in order to show this motion in Figs. 7 b)-7 f). Once the capsule acquires a symmetric geometry, i.e., the parachute-like shape, the tank-treading motion stops.

4.3. Rheology of RBCs

In large arteries and veins, the concentration of RBCs acquires a nearly constant value with average 45%. However, in microcirculation, the concentration of RBCs varies strongly between different vessels due to the so-called plasma skimming effect [72]. In this Section, we consider different numbers of RBCs which are, in all cases, evenly distributed in the parabolic flow defined in Section 4.1. Our aim is to analyze important hemorheological properties such as, e.g., the Fåhræus and the Fåhræus-Lindqvist effects.

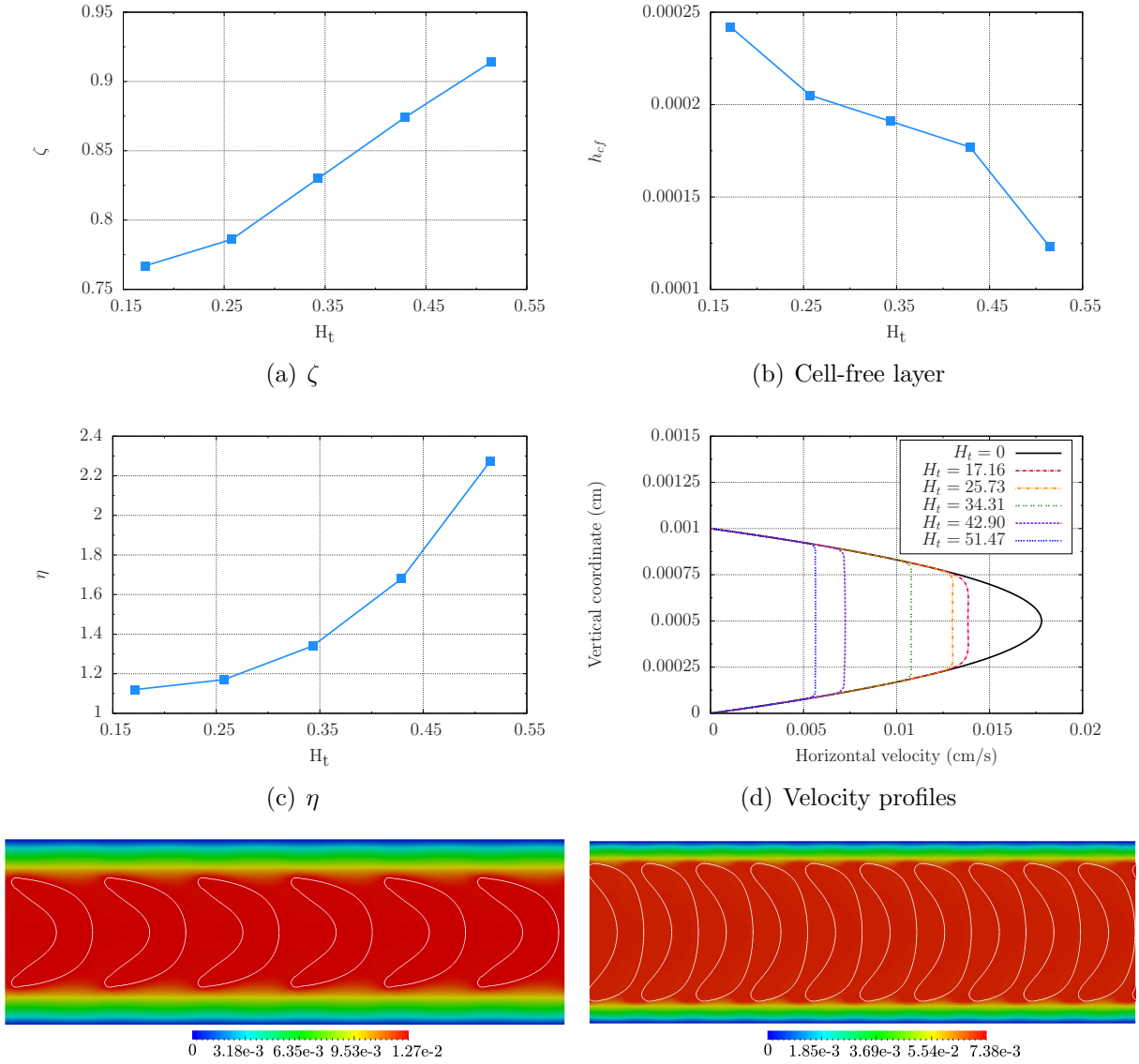

(a) ζ (b) Cell-free layer

(c) η (d) Velocity profiles

(e) $H_t = 0.2573$ (f) $H_t = 0.4290$

Figure 8: *In silico* evaluation of hemorheological properties of blood. (a) Fåhræus effect. As the concentration of RBCs increases, the difference between the mean velocity of RBCs and the mean velocity of blood plasma diminishes. (b) Thickness of the cell-free layer with respect to the tube hematocrit. (c) Fåhræus-Lindqvist effect. The presence of RBCs increases the apparent viscosity of blood. (d) Blunt velocity profiles for different concentrations of RBCs. (e) Velocity magnitude and deformed RBC shapes for $H_t = 0.2573$. (f) Velocity magnitude and deformed RBC shapes for $H_t = 0.4290$.

There are two different ways to measure the concentration of RBCs which are the tube hematocrit (H_t) and the discharge hematocrit (H_d). In a two-dimensional setting, H_t is the ratio of the area enclosed by the RBCs to the blood area and H_d is the ratio of the RBCs flow to the blood flow. In this Section we consider five cases: four RBCs ($H_t = 0.1716$), six RBCs ($H_t = 0.2573$), eight RBCs ($H_t = 0.3431$), ten RBCs ($H_t = 0.4290$), and twelve RBCs ($H_t = 0.5147$). In microcirculation, (H_t) and (H_d) are significantly different and this phenomenon is known as Fåhræus effect. Thus, we define ζ as

$$\zeta = \frac{H_t}{H_d} = \frac{v_{RBCs}}{v_m}, \tag{23}$$

where v_{RBCs} is the mean velocity of RBCs and v_m is the mean velocity of blood. It is known that ζ depends on the concentration of RBCs, the tube diameter (width in our two-dimensional setting), and the strength of the flow. Fig. 8 a) plots the values of ζ for the five different tube hematocrits considered. In accordance with the empirical laws obtained from *in vitro* and *in vivo* experiments [73, 74, 75], ζ increases with the value of H_t. The Fåhræus effect is a consequence of the different mean velocities of RBCs and blood plasma. These two velocities are significantly different in small tubes due to the fact that RBCs tend to travel in the central region of the tube where the velocity is higher. Furthermore, a cell-free layer is known to develop in the boundary of the tube [76]. The thickness of the cell-free layer (h_{cf}) is plotted in Fig. 8 b) for the five different tube hematocrits considered.

In small tubes, the presence of RBCs affects the flow resistence for a certain pressure gradient, i.e., blood behaves as a non-Newtonian fluid where the viscosity is no longer constant. This phenomenon is known as Fåhræus-Lindqvist effect. We define η as the ratio of the blood plasma flow, i.e., the flow of a simulation where only blood plasma is considered (Q_P) to the blood flow, i.e., the flow considering both blood plasma and RBCs (Q). Thus,

$$\eta = \frac{Q_P}{Q} = \frac{v_P}{v_m}, \tag{24}$$

where v_P is the mean velocity of the flow when only blood plasma is considered in the simulation. The value of η depends on the concentration of RBCs, the tube diameter, and the strength of the flow. The parameter η is often called relative apparent viscosity since a Newtonian fluid with viscosity $\eta\mu$ would have the same mean velocity than blood for the particular pressure gradient and tube width considered. Fig. 8 c) plots the values of η for the five tube hematocrits considered. Consistently with empirical laws obtained from *in vitro* and *in vivo* experiments [73, 74, 75], η increases with the value of H_t. We have also computed the velocity profiles once the RBCs have acquired a nearly constant shape. The results for blood plasma and the considered tube hematocrits are plotted in Fig. 8 d). As observed in [77], the velocity develops a blunt profile due to the presence of the RBCs. Finally, Figs. 8 e) and f) show the deformed RBC shapes at time $t = 1$ s for $H_t = 0.2573$ and $H_t = 0.4290$, respectively.

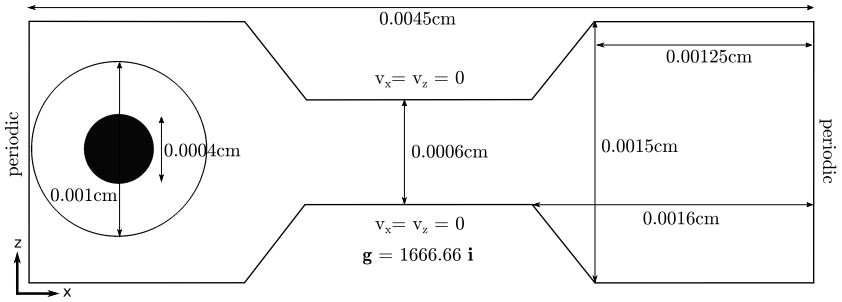

Figure 9: Circulating tumor cell going through a tube narrowing. Problem description of our two-dimensional setting.

4.4. CTC passing through a channel narrowing

In this Section, we consider a CTC going through a narrowing. The computational domain is depicted in Fig. 9. The flow is driven by the forcing $\boldsymbol{g} = (1666.66 \text{ dyn/cm}^3, 0 \text{ dyn/cm}^3)$. No-slip boundary conditions are applied in the vertical direction and periodic boundary conditions are applied in the horizontal direction. The CTC is modeled using a compound capsule. The membrane is a hollow circle with radius $r_m = 0.0005$ cm and thickness $h = 5 \cdot 10^{-7}$ cm. The inclusion is a circle of radius $r_i = 0.0002$ cm. The remaining physical parameters are: $\mu = 0.012$ g/(cm s), $\rho_1 = 1.025$ g/cm^3, $\rho_2 = 1.1$ g/cm^3, $G_m = 2500$ dyn/cm^2, $G_i = 10$ dyn/cm^2.

An Eulerian mesh with 384×128 cubic NURBS elements is used to represent the channel. Lagrangian meshes with 1×768 and 40×192 quadratic NURBS elements are used to represent the membrane and the inclusion, respectively. The time step used in the simulation is $\Delta t = 0.00025$ s.

Fig. 10 plots the velocity magnitude along with the streamlines at different time steps. These snapshots describe how the CTC deforms in order to pass through the tube narrowing. The velocity of the flow decreases while the CTC is inside of the narrowing. Moreover, The highest deformation of the nucleus takes place when the CTC is about to leave the narrowing; see Fig. 10 e). The CTC creates two recirculation regions when it is entering the narrowing as shown in Figs. 10 b) and c). Recirculation regions appear as well when the CTC is leaving the narrowing; see Figs. 10 e) and f). Due to the symmetry of the simulation, there is no TT motion of the membrane at any time.

5. Conclusions and future work

This paper shows that our NURBS-based immersed FSI method is able to capture the behavior of capsules under different flow conditions as long as the incompressibility constraint is adequately satisfied close to the fluid-solid interface. In order to do so, a parameter sweep needs to be performed in advance so as to find a good balance between constraint accuracy, convergence of the solution and computational efficiency. Our results, which are in agreement with experimental and numerical works [16, 71, 74, 75, 76, 77], show that capsules, modeled as solid-shell NURBS elements, are good numerical proxies for red blood cells.

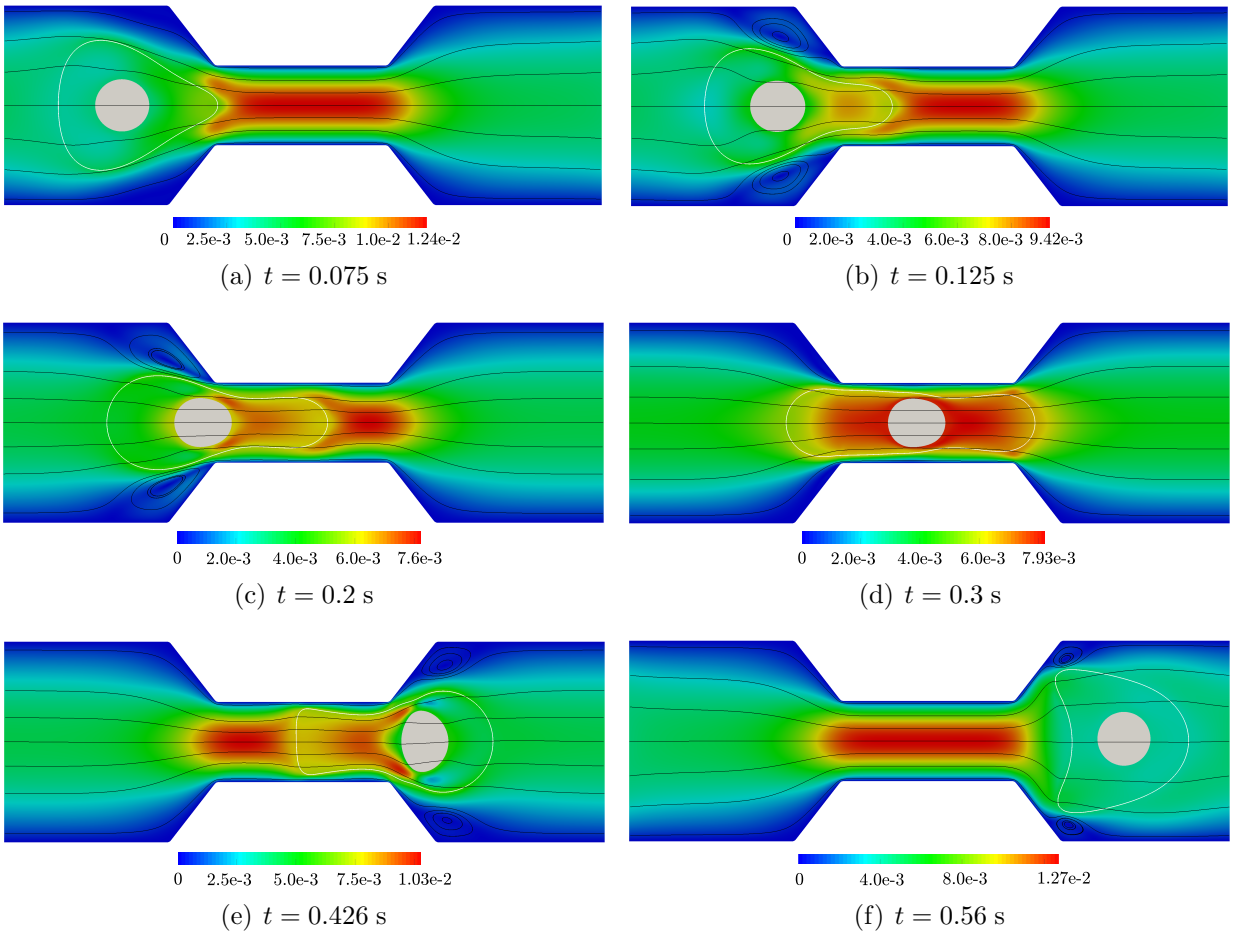

(a) $t = 0.075$ s (b) $t = 0.125$ s (c) $t = 0.2$ s (d) $t = 0.3$ s (e) $t = 0.426$ s (f) $t = 0.56$ s

Figure 10: Snapshots of the velocity magnitude along with the streamlines for a CTC going through a tube narrowing. Note the different scale for each time. The highest deformation of the nucleus appears when the CTC is about to leave the narrowing. The velocity decreases while the CTC is passing through the narrowing. Recirculation regions appear when the CTC is entering and leaving the narrowing.

Inspired by the compound vesicle model presented in [16], we propose hyperelastic compound capsules as a numerical proxy for nucleated cells embedded in flow, such as, e.g., WBCs and CTCs. Our results for the dependence of the inclination angle and tank-treading frequency with the filling fraction are in agreement with results for compound vesicles [16]. Additionally, our geometrically-flexible FSI approach enables us to consider a channel narrowing and analyze how a CTC passes through it. A deeper understanding of this process may provide ideas to improve existent techniques of CTC sorting [78].

Although we have focused on WBCs and CTCs, hyperelastic compound capsules can also be of interest to predict the behavior of composite core-shell microparticles, which can in turn help to understand the mechanical behavior of analagous biomaterials, such as liposomes [79]. The fact that a compound capsule accounts for mechanical strains of the shell and deformability of the nucleus is a first step to better characterize the mechanical

behavior of cells. Recent developments in microfluidics have shown the importance of cell deformability as a biomarker, allowing for metastatic cancer cells to be separated from blood cells, benign cancer cells and normal tissue cells from the same origin by means of inertial fluid effects [80]. In this regard, we believe that the combination of our immersed FSI method, which does not neglect inertial effects, with compound capsules looks highly promising to model these systems, even though more rigorous validation is required. Further improvements of this work include extending the FSI model to be able to handle different viscosities for the fluid inside and outside the membrane, comparing different material models for the membrane, and studying the interaction between RBCs and CTCs in microcirculation.

Acknowledgements

HG, HC and CB-C were partially supported by the European Research Council through the FP7 Ideas Starting Grant (project # 307201). HG was also partially supported by Xunta de Galicia, and by Ministerio de Economía y Competitividad (contract # DPI2013-44406-R). The last two grants are cofinanced with FEDER funds. This support is gratefully acknowledged. We acknowledge the open source scientific libraries PETSc, PetIGA, and their developers.

References

[1] R. Fåhræus, T. Lindqvist, The viscosity of the blood in narrow capillary tubes, American Journal of Physiology–Legacy Content 96 (3) (1931) 562–568.

[2] T. Fischer, M. Stohr-Lissen, H. Schmid-Schonbein, The red cell as a fluid droplet: tank tread-like motion of the human erythrocyte membrane in shear flow, Science 202 (1978) 894–896.

[3] Y. C. Fung, Biomechanics, Springer, New York, 1990.

[4] J. B. Freund, Numerical simulation of flowing blood cells, Annual review of fluid mechanics 46 (2014) 67–95.

[5] D. Abreu, M. Levant, V. Steinberg, U. Seifert, Fluid vesicles in flow, Advances in colloid and interface science 208 (2014) 129–141.

[6] S. K. Veerapaneni, D. Gueyffier, D. Zorin, G. Biros, A boundary integral method for simulating the dynamics of inextensible vesicles suspended in a viscous fluid in 2D, Journal of Computational Physics 228 (7) (2009) 2334 – 2353.

[7] S. K. Veerapaneni, D. Gueyffier, G. Biros, D. Zorin, A numerical method for simulating the dynamics of 3D axisymmetric vesicles suspended in viscous flows, Journal of Computational Physics 228 (19) (2009) 7233 – 7249.

[8] C. Pozrikidis, Modeling and simulation of capsules and biological cells, CRC Press, 2003.

[9] G. Késmárky, P. Kenyeres, M. Rábai, K. Tóth, Plasma viscosity: a forgotten variable, Clinical hemorheology and microcirculation 39 (1–4) (2008) 243–246.

[10] H. W. Hou, M. E. Warkiani, B. L. Khoo, Z. R. Li, R. A. Soo, D. S.-W. Tan, W.-T. Lim, J. Han, A. A. S. Bhagat, C. T. Lim, Isolation and retrieval of circulating tumor cells using centrifugal forces, Scientific Reports 3 (2013) 1259.

[11] M. E. Warkiani, B. L. Khoo, L. Wu, A. K. P. Tay, A. A. S. Bhagat, J. Han, C. T. Lim, Ultra-fast, label-free isolation of circulating tumor cells from blood using spiral microfluidics, Nat. Protocols 11 (1) (2016) 134–148.

[12] T. J. R. Hughes, G. Feijóo, L. Mazzei, J.-B. Quincy, The variational multiscale method - A paradigm for computational mechanics, Computer Methods in Applied Mechanics and Engineering 166 (1998) 3–24.

[13] T. J. R. Hughes, G. Sangalli, Variational multiscale analysis: The fine-scale Green's function, projection, optimization, localization, and stabilized methods, SIAM Journal on Numerical Analysis 45 (2007) 539–557.

[14] Y. Bazilevs, V. M. Calo, J. A. Cottrell., T. J. R. Hughes, A. Reali, G. Scovazzi, Variational multiscale residual-based turbulence modeling for large eddy simulation of incompressible flows, Computer Methods in Applied Mechanics and Engineering 197 (2007) 173–201.

[15] R. Tran-Son-Tay, G. B. Nash, Hemorheology and hemodynamics, IOS Press, Amsterdam, 2007.

[16] S. K. Veerapaneni, Y.-N. Young, P. M. Vlahovska, J. Bławzdziewicz, Dynamics of a compound vesicle in shear flow, Physical review letters 106 (15) (2011) 158103.

[17] P. Koumoutsakos, I. Pivkin, F. Milde, The fluid mechanics of cancer and its therapy, Annual Review of Fluid Mechanics 45 (2013) 325–355.

[18] Y. Liu, L. Zhang, X. Wang, W. K. Liu, Coupling of Navier-Stokes equations with protein molecular dynamics and its application to hemodynamics, International Journal for Numerical Methods in Fluids 46 (2004) 1237–1252.

[19] Y. Liu, W. K. Liu, Rheology of red blood cell aggregation by computer simulation, Journal of Computational Physics 220 (2006) 139–154.

[20] W. K. Liu, S. Jun, Y. F. Zhang, Reproducing kernel particle methods, International Journal for Numerical Methods in Fluids 20 (8-9) (1995) 1081–1106.

[21] W. K. Liu, S. Jun, S. Li, J. Adee, T. Belytschko, Reproducing kernel particle methods for structural dynamics, International Journal for Numerical Methods in Engineering 38 (1995) 1655–1679.

[22] S. Lipton, J. Evans, Y. Bazilevs, T. Elguedj, T. J. R. Hughes, Robustness of isogeometric structural discretizations under severe mesh distortion, Computer Methods in Applied Mechanics and Engineering 199 (2010) 357–373.

[23] H. Casquero, C. Bona-Casas, H. Gomez, A NURBS-based immersed methodology for fluid-structure interaction, Computer Methods in Applied Mechanics and Engineering 284 (2015) 943–970.

[24] H. Casquero, L. Liu, C. Bona-Casas, Y. Zhang, H. Gomez, A hybrid variational-collocation immersed method for fluid-structure interaction using unstructured T-splines, International Journal for Numerical Methods in Engineering 105 (11) (2016) 855–880.

[25] F. Auricchio, L. Beirao Da Veiga, T. J. R. Hughes, A. Reali, G. Sangalli, Isogeometric collocation methods, Mathematical Models and Methods in Applied Sciences 20 (2010) 2075–2107.

[26] H. Casquero, L. Liu, Y. Zhang, A. Reali, H. Gomez, Isogeometric collocation using analysis-suitable T-splines of arbitrary degree, Computer Methods in Applied Mechanics and Engineering 301 (2016) 164 – 186.

[27] D. Schillinger, J. Evans, A. Reali, M. Scott, T. J. R. Hughes, Isogeometric collocation: Cost comparison with Galerkin methods and extension to adaptive hierarchical NURBS discretizations, Computer Methods in Applied Mechanics and Engineering 267 (2013) 170–232.

[28] H. Gomez, A. Reali, G. Sangalli, Accurate, efficient, and (iso)geometrically flexible collocation methods for phase-field models, Journal of Computational Physics 262 (2014) 153–171.

[29] I. Babuška, Error-bounds for finite element method, Numerische Mathematik 16 (4) (1971) 322–333.

[30] F. Brezzi, On the existence, uniqueness and approximation of saddle-point problems arising from lagrangian multipliers, ESAIM: Mathematical Modelling and Numerical Analysis 8 (1974) 129–151.

[31] H. Gomez, L. De Lorenzis, The variational collocation method, Computer Methods in Applied Mechanics and Engineering, DOI: 10.1016/j.cma.2016.06.003.

[32] D. Kamensky, M.-C. Hsu, D. Schillinger, J. A. Evans, A. Aggarwal, Y. Bazilevs, M. S. Sacks, T. J. R. Hughes, An immersogeometric variational framework for fluid-structure

interaction: Application to bioprosthetic heart valves, Computer Methods in Applied Mechanics and Engineering 284 (2015) 1005–1053.

[33] J. A. Cottrell, T. J. R. Hughes, Y. Bazilevs, Isogeometric Analysis Toward Integration of CAD and FEA, Wiley, 2009.

[34] M.-C. Hsu, D. Kamensky, Y. Bazilevs, M. Sacks, T. J. R. Hughes, Fluid-structure interaction analysis of bioprosthetic heart valves: Significance of arterial wall deformation, Computational Mechanics 54 (2014) 1055–1071.

[35] M.-C. Hsu, D. Kamensky, F. Xu, J. Kiendl, C. Wang, M. Wu, J. Mineroff, A. Reali, Y. Bazilevs, M. Sacks, Dynamic and fluid-structure interaction simulations of bioprosthetic heart valves using parametric design with T-splines and Fung-type material models, Computational Mechanics 55 (6) (2015) 1211–1225.

[36] L. Zhang, A. Gerstenberger, X. Wang, W. K. Liu, Immersed finite element method, Computer Methods in Applied Mechanics and Engineering 193 (2004) 2051–2067.

[37] W. K. Liu, Y. Liu, D. Farrell, L. Zhang, X. Wang, Y. Fukui, N. Patankar, Y. Zhang, C. Bajaj, J. Lee, J. Hong, X. Chen, H. Hsu, Immersed finite element method and its applications to biological systems, Computer Methods in Applied Mechanics and Engineering 195 (2006) 1722–1749.

[38] K. Jansen, C. Whiting, G. Hulbert, Generalized-α method for integrating the filtered navier-stokes equations with a stabilized finite element method, Computer Methods in Applied Mechanics and Engineering 190 (2000) 305–319.

[39] T. E. Tezduyar, S. Sathe, Modelling of fluid-structure interactions with the space-time finite elements: Solution techniques, International Journal for Numerical Methods in Fluids 54 (6-8) (2007) 855–900.

[40] Y. Bazilevs, K. Takizawa, T. E. Tezduyar, Computational fluid-structure interaction: methods and applications, John Wiley & Sons, 2012.

[41] P. R. Brune, M. G. Knepley, B. F. Smith, X. Tu, Composing scalable nonlinear algebraic solvers, SIAM Review 57 (4) (2015) 535–565.

[42] Y. Saad, M. H. Schultz, Gmres: A generalized minimal residual algorithm for solving nonsymmetric linear systems, SIAM Journal on scientific and statistical computing 7 (1986) 856–869.

[43] C. Michler, E. van Brummelen, R. de Borst, Error-amplification analysis of subiteration-preconditioned gmres for fluid-structure interaction, Computer Methods in Applied Mechanics and Engineering 195 (17-18) (2006) 2124–2148.

[44] L. Dalcin, N. Collier, P. Vignal, A. Crtes, V. Calo, PetIGA: A framework for high-performance isogeometric analysis, Computer Methods in Applied Mechanics and Engineering 308 (2016) 151 – 181.

[45] P. A. Vignal, N. Collier, V. M. Calo, Phase field modeling using PetIGA, Procedia Computer Science 18 (2013) 1614–1623.

[46] M. Bernal, V. M. Calo, N. Collier, G. Espinosa, F. Fuentes, J. Mahecha, Isogeometric analysis of hyperelastic materials using PetIGA, Procedia Computer Science 18 (2013) 1604–1613.

[47] S. Balay, M. F. Adams, J. Brown, P. Brune, K. Buschelman, V. Eijkhout, W. D. Gropp, D. Kaushik, M. G. Knepley, L. C. McInnes, K. Rupp, B. F. Smith, H. Zhang, PETSc Web page, `http://www.mcs.anl.gov/petsc` (2014).

[48] S. Balay, M. F. Adams, J. Brown, P. Brune, K. Buschelman, V. Eijkhout, W. D. Gropp, D. Kaushik, M. G. Knepley, L. C. McInnes, K. Rupp, B. F. Smith, H. Zhang, PETSc users manual, Argonne National Laboratory (ANL-95/11 - Revision 3.4). URL `http://www.mcs.anl.gov/petsc`

[49] K. Singh, J. Williams, Application of the additive schwarz method to large scale poisson problems, Communications in numerical methods in engineering 20 (3) (2004) 193–205.

[50] H. Schmid-Schönbein, R. Wells, Fluid drop-like transition of erythrocytes under shear, Science 165 (3890) (1969) 288–291.

[51] H. Goldsmith, J. Marlow, Flow behaviour of erythrocytes. i. rotation and deformation in dilute suspensions, Proceedings of the Royal Society of London B: Biological Sciences 182 (1068) (1972) 351–384.

[52] H. Basu, A. K. Dharmadhikari, J. A. Dharmadhikari, S. Sharma, D. Mathur, Tank treading of optically trapped red blood cells in shear flow, Biophysical journal 101 (7) (2011) 1604–1612.

[53] J. Kiendl, M.-C. Hsu, M. C. Wu, A. Reali, Isogeometric Kirchhoff–Love shell formulations for general hyperelastic materials, Computer Methods in Applied Mechanics and Engineering 291 (2015) 280–303.

[54] H. Casquero, L. Liu, Y. Zhang, A. Reali, J. Kiendl, H. Gomez, Arbitrary-degree T-splines for isogeometric analysis of fully nonlinear Kirchhoff-Love shells, Computer Aided Design`doi:10.1016/j.cad.2016.08.009`.

[55] D. A. Fedosov, M. Peltomäki, G. Gompper, Deformation and dynamics of red blood cells in flow through cylindrical microchannels, Soft Matter 10 (24) (2014) 4258–4267.

[56] R. Skalak, N. Ozkaya, , T. C. Skalak, Biofluid mechanics, Annual Review of Fluid Mechanics 21 (1) (1989) 167–200.

[57] R. Skalak, A. Tozeren, R. Zarda, S. Chien, Strain energy function of red blood cell membranes, Biophysical Journal 13 (3) (1973) 245 – 264.

[58] P. Bagchi, R. M. Kalluri, Dynamics of nonspherical capsules in shear flow, Physical Review E 80 (1) (2009) 016307.

[59] Y. Sui, Y. Chew, P. Roy, H. Low, A hybrid method to study flow-induced deformation of three-dimensional capsules, Journal of Computational Physics 227 (12) (2008) 6351 – 6371.

[60] S. Ramanujan, C. Pozrikidis, Deformation of liquid capsules enclosed by elastic membranes in simple shear flow: large deformations and the effect of fluid viscosities, Journal of Fluid Mechanics 361 (1998) 117–143.

[61] T. J. R. Hughes, J. A. Cottrell, Y. Bazilevs, Isogeometric analysis CAD, finite elements, NURBS, exact geometry and mesh refinement, Computacional Methods in Applied Mechanics and Engineering 194 (2005) 4135–4195.

[62] B. Kaoui, J. Harting, C. Misbah, Two-dimensional vesicle dynamics under shear flow: Effect of confinement, Physical Review E 83 (6) (2011) 066319.

[63] M. R. King, K. G. Phillips, A. Mitrugno, T.-R. Lee, A. M. de Guillebon, S. Chandrasekaran, M. J. McGuire, R. T. Carr, S. M. Baker-Groberg, R. A. Rigg, et al., A physical sciences network characterization of circulating tumor cell aggregate transport, American Journal of Physiology-Cell Physiology 308 (10) (2015) C792–C802.

[64] I. Cantat, C. Misbah, Lift force and dynamical unbinding of adhering vesicles under shear flow, Physical review letters 83 (4) (1999) 880.

[65] D. A. Fedosov, J. Fornleitner, G. Gompper, Margination of white blood cells in microcapillary flow, Physical review letters 108 (2) (2012) 028104.

[66] O. K. Baskurt, Handbook of hemorheology and hemodynamics, Vol. 69, IOS press, 2007.

[67] B. Kaoui, T. Krüger, J. Harting, Complex dynamics of a bilamellar vesicle as a simple model for leukocytes, Soft Matter 9 (33) (2013) 8057–8061.

[68] Z. Y. Luo, L. He, B. F. Bai, Deformation of spherical compound capsules in simple shear flow, Journal of Fluid Mechanics 775 (2015) 77–104.

[69] G. Coupier, B. Kaoui, T. Podgorski, C. Misbah, Noninertial lateral migration of vesicles in bounded poiseuille flow, Physics of Fluids (1994-present) 20 (11) (2008) 111702.

[70] G. Danker, P. M. Vlahovska, C. Misbah, Vesicles in poiseuille flow, Physical review letters 102 (14) (2009) 148102.

[71] J. L. McWhirter, H. Noguchi, G. Gompper, Deformation and clustering of red blood cells in microcapillary flows, Soft Matter 7 (22) (2011) 10967–10977.

[72] A. Krogh, The anatomy and physiology of capillaries, Vol. 18, Yale University Press, 1922.

[73] R. Fåhraeus, The suspension stability of the blood, Physiological Reviews 9 (2) (1929) 241–274.

[74] S. Chien, S. Usami, R. Skalak, Blood flow in small tubes, Handbook of physiology, section 2 (1984) 217–249.

[75] A. R. Pries, T. W. Secomb, Microvascular blood viscosity in vivo and the endothelial surface layer, American Journal of Physiology-Heart and Circulatory Physiology 289 (6) (2005) H2657–H2664.

[76] P. Olla, Simplified model for red cell dynamics in small blood vessels, Physical review letters 82 (2) (1999) 453.

[77] P. Bagchi, Mesoscale simulation of blood flow in small vessels, Biophysical journal 92 (6) (2007) 1858–1877.

[78] Z. Zhang, J. Xu, B. Hong, X. Chen, The effects of 3d channel geometry on ctc passing pressure - towards deformability-based cancer cell separation, Lab Chip 14 (2014) 2576–2584.

[79] T. Kong, L. Wang, H. M. Wyss, H. C. Shum, Capillary micromechanics for core-shell particles, Soft Matter 10 (2014) 3271–3276.

[80] S. C. Hur, N. K. Henderson-MacLennan, E. R. B. McCabe, D. Di Carlo, Deformability-based cell classification and enrichment using inertial microfluidics, Lab Chip 11 (2011) 912–920.